

Gastric histopathology image segmentation using a hierarchical conditional random field

Changhao Sun^{a,b}, Chen Li^{a,b,*}, Jinghua Zhang^{a,b}, Shiliang Ai^{a,b}, Hao Chen^{a,b}, Frank Kulwa^{a,b}, Xiaoyan Li^c, Tao Jiang^d

^aNortheastern University, Microscopic Image and Medical Image Analysis Group, MBIE College, Shenyang, P.R. China, 110819

^bNortheastern University, Engineering Research Center of Medical Imaging and Intelligent Analysis, Ministry of Education, Shenyang, P.R. China, 110819

^cChina Medical University, Department of Pathology, Cancer Hospital, Liaoning Cancer Hospital and Institute, Shenyang, P.R. China, 110042

^dChengdu University of Information Technology, Control Engineering College, Chengdu, P.R. China, 610103

Abstract. The existing convolutional neural networks (CNNs) applied in the intelligent diagnosis of gastric cancer usually focus on individual characteristics and network framework without a policy to depict the integral information. Particularly, conditional random field (CRF), an effectual and stable algorithm for analysing the contents of complicated images, is able to characterize the spatial relation in images. In this paper, a novel hierarchical conditional random field (HCRF) model based gastric histopathology image segmentation (GHIS) method is proposed, which can automatically localize abnormal (cancer) regions in gastric histopathology images obtained by the optical microscope to assist histopathologists in medical work. The HCRF model is built up with higher order potentials, including pixel-level and patch-level potentials, and graph-based post-processing is applied to further improve our segmentation performance. We retrain a CNN to build up our pixel-level potentials and fine-tune another three CNNs to build up our patch-level potentials for abundant spatial segmentation information. In the experiment, segmentation accuracy, recall and specificity of 78.91%, 65.59%, and 81.33% are achieved on a hematoxylin and eosin (H&E) stained gastric histopathological dataset with 560 images. Our study demonstrates high segmentation performance achieved by the HCRF model and shows effectiveness and future potential of the proposed GHIS method.

Keywords: Image Segmentation, Gastric Cancer, Histopathology Image, Conditional Random Field, Convolutional Neural Network, Feature Extraction.

*Chen Li, lichen201096@hotmail.com

1 Introduction

Gastric cancer is one of the five commonest sorts of malignant tumors in human being on the basis of the World Health Organization (WHO) reports. Patients with gastric cancer accounts for 7% of all cancer cases and 9% of cancer death cases. Almost 75% of new cases occur in Asia, and more than 40% occur in China.¹ The disease specific survival is practically 12 months and 90% of gastric cancer cases die within the first five years. Since gastric cancer is one of the most aggressive and deadliest cancer, it is very important for medical professionals to accurately estimate patient

prognoses.²

Recently, image analysis systems have found great use in the intelligent diagnosis of gastric cancer, where a variety of deep learning (DL) methods, especially convolutional neural networks (CNNs), are developed and applied to gastric histopathology image segmentation (GHIS) and classification tasks.³ From VGG-16⁴ to fully convolutional networks (FCNs),⁵ from FCNs to DeepLab,⁶ the DL algorithms are continually in progress in the GHIS field. Nevertheless, the current methods routinely concentrate on separate characteristics and network frameworks, such as layer numbers and network structures, lacking a policy to depict the integral information. Hence, for achieving a higher computing performance, some superior algorithms are designed to incorporate these individual existing approaches. Particularly, conditional random field (CRF), an effective and stable algorithm for analysing the contents of complicated images, is able to represent the spatial relation in gastric histopathological images obtained by optical microscopes, which are an admixture of the complex nuclei, cytoplasm, interstitial and tissue fluids. Meanwhile, the pathological doctors are usually too busy to annotate all abnormal (cancer) regions in gastric histopathology image, it is necessary to design an efficient multi-object segmentation method. Thus, a novel hierarchical conditional random field (HCRF) model is proposed to complete the GHIS task. Additionally, the observation of histionic optical features in a gastric histopathological image can be on patch-scale and applying the whole image to train the classifier is not efficient and wasting computing resource, it is better to use the patches cut from the image rather than the whole image to train the model.⁷ Fig. 1 indicates the workflow of the proposed HCRF model.

As shown in Fig. 1, we can see that: First, Data Input: To train the proposed HCRF model, original gastric carcinoma histopathological images (original images) and their corresponding ground truth images (GT images) are used as training and validation sets for a supervised learning pro-

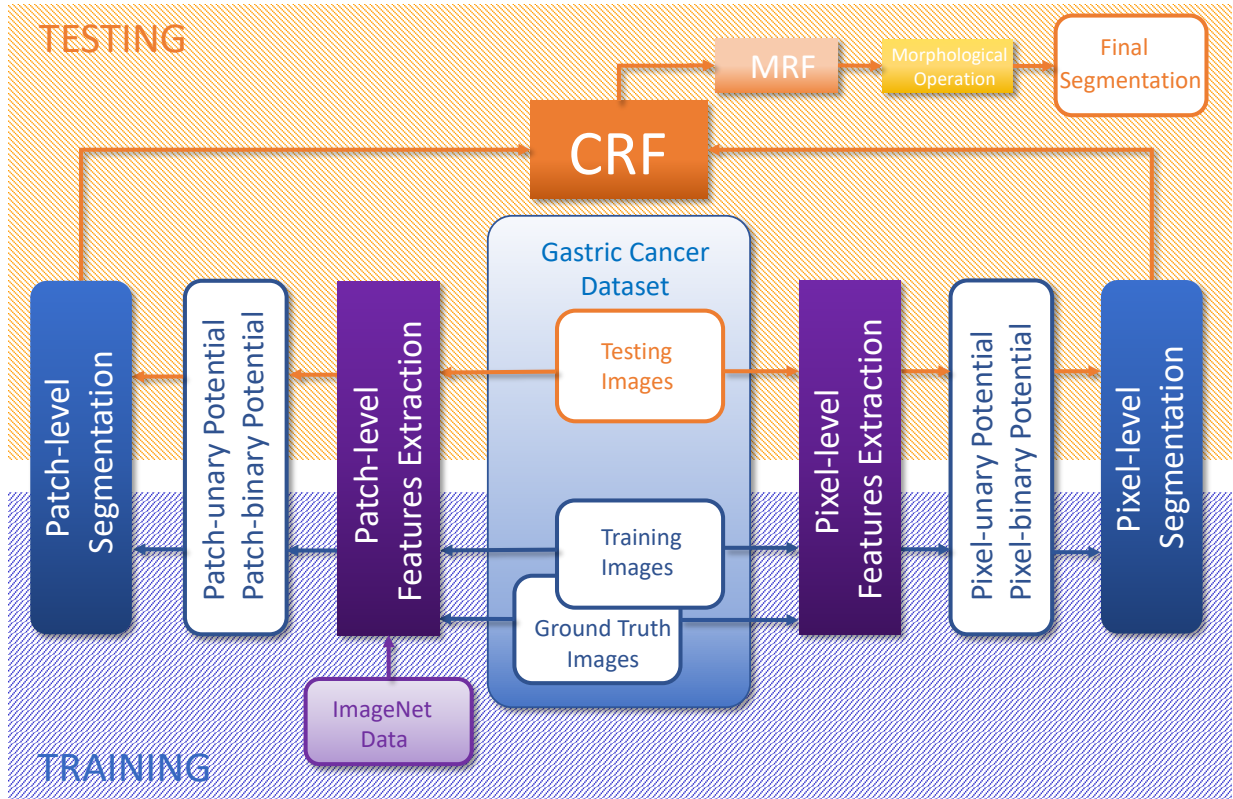


Fig 1 The workflow of the proposed hierarchical conditional random field (HCRF) model for the gastric histopathology image segmentation (GHIS).

cess. The size of the original images is 2048×2048 pixels. The pixels in GT images are 1 (foreground abnormal regions, white) and 0 (background normal regions, black). Especially, some pre-processing is carried out: (1) In pixel-level training, we first augment the training and validation sets by flipping the original and GT images horizontally and vertically, and rotating the images to 90, 180, 270 degrees. Then we mesh the images into patches (256×256 pixels). (2) In patch-level training, we mesh the original and GT images into patches (64×64 pixels) and the size of each patch is 4096 pixels. When the sum of the pixel values in a GT image is over 2048, we give the corresponding original image patch a foreground label (1, white); otherwise we give it a background label (0, black). However, when we do this approximate processing, the foreground image patches are much less than the background image patches. Hence, in order to balance the data during training, we specially augment the foreground image patches by flipping horizontally

and vertically, and rotating the images to 90, 180, 270 degrees in the training and validation sets.

Second, HCRF Model: To build our HCRF based image segmentation model, we focus on four potentials, including pixel-unary, pixel-binary, patch-unary and patch-binary potentials. (1) In pixel-level, we extract pixel-level features and get the pixel-unary and pixel-binary segmentation results. (2) In patch-level, we first extract patch-level features and get three patch-unary and three patch-binary segmentation results. Then, we obtain the optimized patch-unary and patch-binary segmentation results to enhance the segmentation performance. (3) Based on the pixel-unary, pixel-binary, patch-unary and patch-binary potentials, we generate the main body of our HCRF image segmentation model. (4) In addition, we apply Markov random field (MRF)⁸ and morphological operations⁹ to further optimize the segmentation result.

Third, System Evaluation: To evaluate the effectiveness of the proposed HCRF based image segmentation method, we input test images to it and calculate multiple indexes for an overall assessment.

There are three main contributions of our work: First, we heuristically apply a CRF framework to a new research field of the GHIS. Second, we propose a novel HCRF model using higher order potentials in this paper. Thirdly, we obtain a high segmentation performance by the HCRF model for gastric histopathology images.

This paper is structured as follows: Sec. 2 gives a summary of the related. Sec. 3 illustrates how the HCRF model is built up. Sec. 4 presents the experimental results of the proposed HCRF. Sec. 5 compares our method to the previous GHIS studies. Finally, Sec. 6 gives a brief conclusion and the future work.

2 Related Work

We summarize the related works as follows: Sec. 2.1 introduces the basic knowledge of gastric cancer. Sec. 2.2 discusses image segmentation techniques in gastric histopathology field. Sec. 2.3 is about the applications of CRFs. Sec. 2.4 concludes the related DL methods.

2.1 Gastric Cancer

Gastric cancer is the amassment of abnormal cells that can be malignant or cancerous, forming tumors in the stomach. It is the second most prevalent malignancy in males after lung cancer and the third in women after lung and breast cancer. On the basis of the report from WHO, nearly 800000 people die of the gastric cancer each year.¹⁰ Most of the gastric cancer cases occur in the east Asia countries such as Japan and China. Particularly, the number of gastric cancer patients accounts for approximate 30% of other types of cancer in Japan. Meanwhile, among countries in America, the gastric cancer cases also grow year by year. A meticulous examination of hematoxylin and eosin (H&E) stained tissue slices under a optical microscope by pathologists is necessary during the diagnosis of gastric cancer. But, the microscopic examination is subjective, tedious and time-consuming. Besides, the screening process regularly takes 5–10 minutes for one slide. For obtaining a high work quality, the maximum number of samples that a pathologist can analyse is 70 a day.¹¹ In case of leaving out any diagnostic areas, full attention are invariably required in the procedure. So, having a pathologist to screen and diagnose gastric cancer slides is a chief matter. With the evolution of artificial intelligence (AI), a lot of AI algorithms are increasingly utilized to the disease diagnose,^{3,12} prompting us to develop an intelligent diagnose system which can effectively and accurately analyse gastric cancer slides.¹³

2.2 Image Segmentation in Gastric Histopathology Research

There exists two kind of tasks in gastric histopathology image segmentation which are cell-scale and tissue-scale segmentation.^{3,14} In cell-scale segmentation,^{10,15-17} they concentrate on the nuclei information. In tissue-scale segmentation,¹⁸⁻²² the whole abnormal areas are of interest instead of the separated cells. In this paper, our HCRF model is developed for tissue-scale segmentation.

In,¹⁰ a multi-stage approach aims to segment the nuclei of gastric cancer from a histopathology image. First, a contour based minimum-model method including six main steps is used in the gastric cancer nuclei segmentation step.¹⁵ Then, color, texture and morphological features are extracted from the segmented nuclei. Thirdly, AdaBoost, an ensemble learning method is utilized to improve the performance of individual classifiers. Lastly, the segmentation results at different resolutions are combined. Finally, an average multi-class classification accuracy of 58.8% is obtained on twelve Her2/neu immunohistochemically stained gastric cancer cases which are converted to H&E stain.

Recently, CNN-based methods are applied to gastric cancer segmentation. In,¹⁶ a three-class CNN algorithm is developed to segment the inside, outside and the boundary of gastric cancer nuclei. First, color normalization is applied as a pre-processing step. Then, a three-class CNN is designed to emphasize the nuclear boundaries. Lastly, three classes of segmented objects are transferred to n -ary nuclear maps for post-processing. In the experiment, a publicly accessible H&E stained dataset of histopathology images with more than 21000 labelled nuclear boundaries is utilized for testing. This dataset covers 7 organs, including stomach and others. For each organ, there are 30 whole slide images (WSIs) in the dataset. Finally, a overall F1-score of 82.67% is obtained.

State-of-the-art networks used in gastric histopathology image segmentation are FCNs. In,¹⁷ an U-Net based FCN is proposed to detect nuclei and corresponding boundaries simultaneously from gastric histopathology image patches. In the experiment, three datasets are tested: The first is the same as that used in,¹⁶ and another two are breast cancer histopathology image datasets. Finally, the F1-scores of 82.7%, 92.3% and 84% are achieved on these three datasets, respectively.

With the advancement of high speed computers, the entire abnormal tissue areas in the digital pathology image can be labelled automatically. In,¹⁸ they use a FCN including two steps for gastric histopathology image classification and segmentation. First, patches extracted from original gastric histopathology images are used to fine-tune the classification CNN. Then the CNN in first step is transformed to a FCN for segmentation. AlexNet and GoogLeNet are used as backbones. Finally, the segmentation accuracies of 65.7% and 78.5% are achieved on 400 images respectively.

In,¹⁹ a network using multi-scale blocks which are similar to Inception architecture for shallow layers and feature pyramid for deep layers is proposed for gastric histopathology image segmentation. Outstanding result of 90.88% F1-score is achieved on 672 gastric histopathology images.

A two-step model for gastric WSI segmentation is proposed in.²⁰ In first step, they design a network to detect discriminative patches. In second step, a recalibrated multi-instance deep learning (RMDL) is used for image-level segmentation. Their two-step method reaches 86.5% classification accuracy on 608 H&E stained and carefully labelled WSIs.

In,²¹ a reiterative training strategy and a particular loss function are utilized for partially annotated gastric histopathology image segmentation. A segmentation accuracy of 91.45% is achieved on 1400 roughly annotated training images, 400 precisely annotated validation images and 100 precisely annotated test images.

In,²² a network using encoder-decoder architecture which is utilized for fusing both low-level

and high-level features, and multi-scale modules is designed. They achieve 91.60% segmentation accuracy on a dataset including 500 carefully annotated gastric histopathology images.

Furthermore, a comparison of the previous GHIS studies mentioned above is shown in Table 11 in Sec. 5.

2.3 Applications of CRFs

In recent years, in order to label and parse sequential message, CRFs are utilized in machine vision²³ and human language comprehension or other biomedical signal processing areas.²⁴ CRFs are effective algorithms to tag part-of-speech, accomplish shallow parsing task,²⁵ recognize named entity,²⁶ find gene and peptide critical functional regions.²⁷ Moreover, CRFs are accessible choices for other machine learning (ML) algorithms, such as the hidden Markov models and recurrent neural network (RNN).²⁸ As for machine vision areas, CRFs also play a great vital role for image classification,²⁹ semantic segmentation²⁸ and post-processing.⁶

CRFs are widely applied in medical image analysing as well. In,³⁰ they design a probabilistic discriminative algorithm based on CRFs to merge the contextual features within functional images. The experimental results reveal that the proposed CRF model is a robust method to detect brain activities from real functional magnetic resonance imaging data.

A segmentation algorithm combining CRFs with a cost-sensitive structure is proposed in.³¹ The experiment indicates that the previous cost-sensitive support vector machine (SVM) results are highly promoted by the proposed method which adds spatial information to the CRFs.

In,^{32,33} a CRF architecture applied in colposcopy images of cervical cancer neoplasia is proposed as an extraction of the domain-specific characteristics of diagnosis which are in the manner

of probability. As a result, locating the abnormal areas is achieved basing upon the relations of tissue and visual information.

Due to the progress of many new DL techniques, more and more studies incorporate DL algorithms, especially CNNs, with CRF models to attain higher performance in image classification and segmentation task. For instance, in,³⁴ an automatic microscopic image classification and segmentation method which is a strongly supervised CRF framework based on DeepLab aims at classifying and segmenting the environmental microorganism images using CNN feature maps. At last, an overall pixel accuracy of 94.2% and a mean average precision of 91.4% are achieved. In another research,³⁵ a weakly supervised multilayer hidden CRF framework with classical ML and DL techniques is designed to classify cervical cancer images, achieving an overall accuracy of 88%. In this study, we propose a HCRF framework with CNNs techniques for the GHIS task, which has not been applied to the problem in this field.

2.4 Related Deep Learning Method

VGG-16³⁶ contains 16 weight layers, consisting of 13 convolution layers and 3 fully connected layers and 5 pooling layers without weights, and it uses convolution kernels with the same size to extract complex features.⁴ Inception-V3 network is based on the Inception-V1 and Inception-V2 networks. Inception-V1 contains inception module with dimension reduction using 1×1 convolution layers and multi-scale filters.³⁷ Inception-V2 further adds batch normalization into the network structure.³⁸ Inception-V3 factorizes the large convolutions into small convolutions and optimizes the Inception module.³⁹ Inception-V3 is more deeper than VGG-16 and uses multi-scale convolution kernels to extract multi-scale spatial features. In order to deal with the network degradation problem and train very deep neural networks, ResNet-50 proposes deep residual learning

strategy using a short-cut connection structure.⁴⁰ U-Net comes from FCNs, using “encode-decode” and “skip connection structures”.³⁶ To seamlessly segment the optional images with large sizes, U-Net applies “overlap-title” algorithm.³⁶ It shows effectiveness in medical image segmentation tasks, for example the works in.^{36,41,42}

3 Method

Firstly, Sec. 3.1 introduces the fundamental definition of CRFs. Afterwards, Sec. 3.2 elaborates on our proposed HCRF model, including pixel-unary, pixel-binary, patch-unary, patch-binary potentials, and their combination.

3.1 Fundamental Definition of CRFs

The basic theorem of CRF is presented in:²⁴ First of all, the observation sequence \mathbf{Y} is a random variable to be labelled, and \mathbf{X} is the random variable of the relative label sequence. Secondly, $G = (V, E)$ is a graph where $\mathbf{X} = (\mathbf{X}_v)_{v \in V}$, whilst \mathbf{X} is indexed by the nodes or vertices of G . V is the array of all sites, which corresponds with the vertices in the related undirected graph G , where edges E construct the interactions among adjacent sites. Therefore, (\mathbf{X}, \mathbf{Y}) is a CRF in case, when conditioned on observation sequence \mathbf{Y} , the random variables \mathbf{X}_v follow the Markov properties with regard to the graph: $p(\mathbf{X}_v | \mathbf{Y}, \mathbf{X}_w, w \neq v) = p(\mathbf{X}_v | \mathbf{Y}, \mathbf{X}_w, w \sim v)$, in which $w \sim v$ implies w and v are neighbours in $G = (V, E)$. These principles indicate the CRF model is an undirected graph in which two disjoint sets \mathbf{X} and \mathbf{Y} are separated from the nodes. In that case, the conditional distribution model is $p(\mathbf{X} | \mathbf{Y})$.

Based on the definition of the random fields in,⁴³ the joint distribution over the label sequence

\mathbf{X} given \mathbf{Y} forms as Eq. (1).

$$p_{\theta}(\mathbf{x}|\mathbf{y}) \propto \exp\left(\sum_{e \in E, k} \lambda_k f_k(e, \mathbf{x}|_e, \mathbf{y}) + \sum_{v \in V, k} \mu_k g_k(v, \mathbf{x}|_v, \mathbf{y})\right), \quad (1)$$

where \mathbf{y} is the observation sequence, \mathbf{x} is the corresponding label sequence, and $\mathbf{x}|_S$ is the set of sections of \mathbf{x} in association with the vertices of sub-graph S . Furthermore, from^{6,28,44} it can be comprehended that a redefinition of Eq. (1) is Eq. (2).

$$p(\mathbf{X}|\mathbf{Y}) = \frac{1}{Z} \prod_C \psi_C(\mathbf{X}_C, \mathbf{Y}), \quad (2)$$

where $Z = \sum_{\mathbf{X}} P(\mathbf{X}|\mathbf{Y})$ is the normalization factor and $\psi_C(\mathbf{X}_C, \mathbf{Y})$ is the potential function over the clique C . The clique C is the subset of the vertices in the undirected graph G , where $C \subseteq V$, in this way, every two different vertices are adjoining.

3.2 Hierarchical Conditional Random Fields

3.2.1 The Architecture of the HCRF Model

Most of CRF models have so far been built up with only unary and binary potentials.^{6,28} Nevertheless, potentials defined on higher order cliques have been verified to be effective in previous studies, such as.^{45,46} Since our concentration is on the optical features in tissue-scale in the gastric histopathological images,⁷ two types of higher order potentials are introduced, one is a patch-unary potential to characterize the information of tissues, the other is a patch-binary potential to depict the surrounding spatial relation among different tissue areas. Consequently, by the fundamental

theorem of CRFs in Sec. 3.1, our HCRF is defined as Eq. (3).

$$\begin{aligned}
p(\mathbf{X}|\mathbf{Y}) = & \frac{1}{Z} \prod_{i \in V} \varphi_i(x_i; \mathbf{Y}; w_V) \prod_{(i,j) \in E} \psi_{(i,j)}(x_i, x_j; \mathbf{Y}; w_E) \\
& \prod_{m \in V_P} \varphi_m(\mathbf{x}_m; \mathbf{Y}; w_m; w_{V_P}) \prod_{(m,n) \in E_P} \psi_{(m,n)}(\mathbf{x}_m, \mathbf{x}_n; \mathbf{Y}; w_{(m,n)}; w_{E_P}),
\end{aligned} \tag{3}$$

where

$$Z = \sum_{\mathbf{X}} \prod_{i \in V} \varphi_i(x_i; \mathbf{Y}) \prod_{(i,j) \in E} \psi_{(i,j)}(x_i, x_j; \mathbf{Y}) \prod_{m \in V_P} \varphi_m(\mathbf{x}_m; \mathbf{Y}) \prod_{(m,n) \in E_P} \psi_{(m,n)}(\mathbf{x}_m, \mathbf{x}_n; \mathbf{Y}), \tag{4}$$

is the normalization factor; V represents a set of all vertices in the graph $G = (V, E)$, corresponding to the image pixels; E represents a set of all edges in the graph G . V_P is one patch divided from an image; E_P represents the surrounding patches of a single patch. The usual clique potential function forms two components: The pixel-unary potential function $\varphi_i(x_i, \mathbf{Y})$ is the measurement of the probability that one pixel vertex i is labelled as $x_i \in \mathbf{X}$, which gets values from a given set of classes \mathbb{L} , given input data \mathbf{Y} ; ³⁴ the pixel-binary potential function $\psi_{(i,j)}(x_i, x_j; \mathbf{X})$ is utilized to characterize the adjacent vertices i and j of the graph G . The spatial contextual relations among them are not only associated with the label of vertex i but also to the label of its neighbouring vertices j . Furthermore, $\varphi_m(\mathbf{x}_m; \mathbf{Y})$ and $\psi_{(m,n)}(\mathbf{x}_m, \mathbf{x}_n; \mathbf{Y})$ are the newly introduced higher order potentials. The patch-unary potential function $\varphi_m(\mathbf{x}_m, \mathbf{Y})$ is the measurement of the probability which a patch vertex m is labelled as \mathbf{x}_m given input data \mathbf{Y} ; the patch-binary potential function $\psi_{(m,n)}(\mathbf{x}_m, \mathbf{x}_n; \mathbf{Y})$ is utilized to present the adjacent vertices m and n in the patch. w_V , w_E , w_{V_P} and w_{E_P} are the weights of the four potentials, $\varphi_i(x_i, \mathbf{Y})$, $\psi_{(i,j)}(x_i, x_j; \mathbf{X})$, $\varphi_m(\mathbf{x}_m, \mathbf{Y})$ and $\psi_{(m,n)}(\mathbf{x}_m, \mathbf{x}_n; \mathbf{Y})$, respectively. w_m and $w_{(m,n)}$ are the weights of the $\varphi_m(\cdot; \mathbf{Y})$ and $\psi_{(m,n)}(\cdot, \cdot; \mathbf{Y})$,

respectively. These weights are used to seek out the largest posterior label $\tilde{\mathbf{X}} = \arg \max_{\mathbf{X}} p(\mathbf{X}|\mathbf{Y})$ and to further improve the image segmentation performance. To give a visualized understanding, the architecture of the proposed HCRF model is presented in Fig. 2.

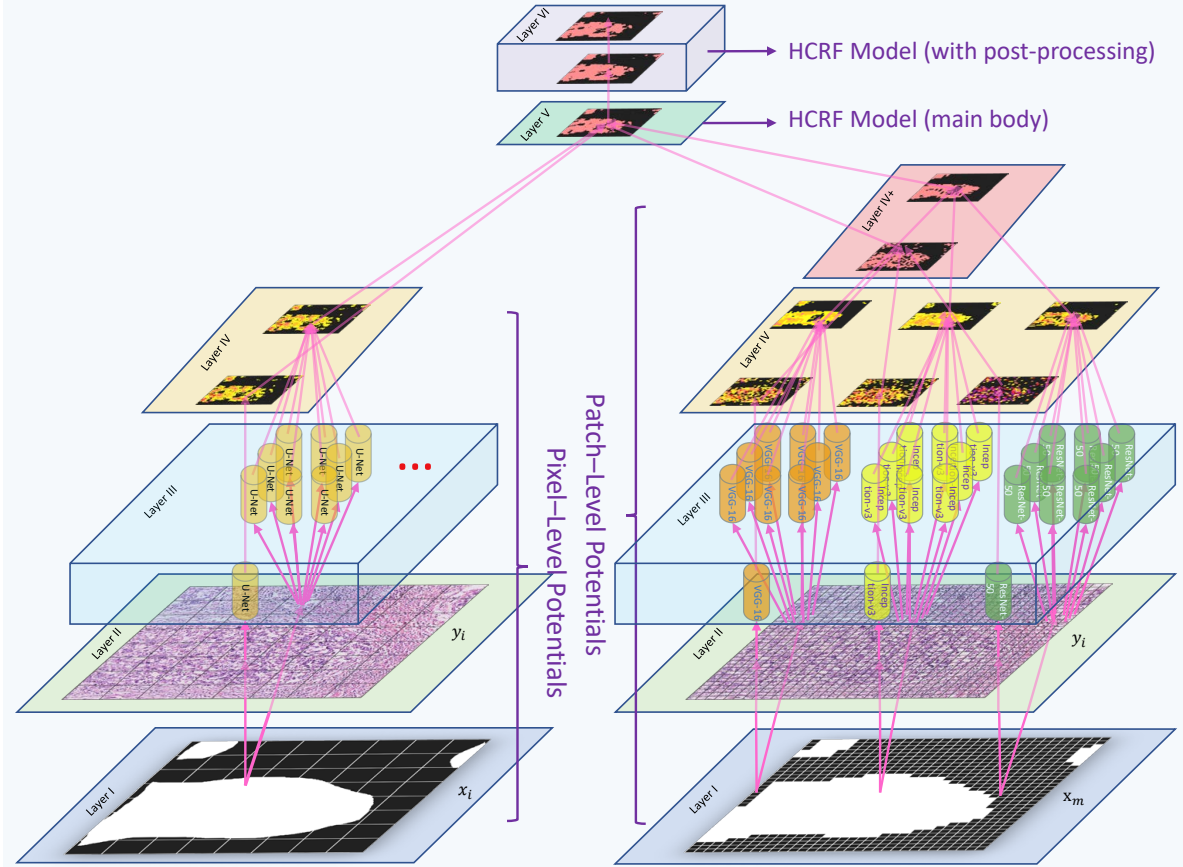


Fig 2 The architecture of the HCRF model. The left branch represents the terms of the pixel-level potentials, and the right branch represents the terms of the patch-level potentials.

From Fig. 2, the architecture of the HCRF model is as follows:

- Layer I presents the real labels x_i of pixels and real labels x_m of patches in a gastric histopathology image.
- Layer II characterizes the original image pixels y_i that match one to one with the pixel labels x_i , and the original image patches y_i that match one to one with the patch labels x_m in Layer I.

- From the pixel-level side, Layer III represents the U-Net, which is applied in pixel-level potentials using images pixels y_i . To this end, we retrain the U-Net using the gastric cancer histopathology images. From the patch-level side, Layer III denotes three types of CNNs that are applied in patch-level potentials using image patches y_i , including VGG-16, Inception-V3 and ResNet-50 networks. First, these three networks are pre-trained on 1.3 million images from ImageNet dataset⁴⁷ with a transfer learning strategy.^{4,5,48} Then, because the images from ImageNet are all natural and daily life pictures, we use the gastric cancer histopathology images to fine-tune the VGG-16, Inception-V3¹⁴ and ResNet-50 networks.
- In Layer IV, we get one type of pixel-unary potential, corresponding to U-Net; and three types of patch-unary potentials, corresponding to VGG-16, Inception-V3 and ResNet-50 networks. In order to obtain the pixel-level binary potentials, we calculate the potentials of the surrounding pixels basing on the layout shown in Fig. 3. Similarly, to obtain the patch-level binary potentials, we calculate the potentials of the image patches which surround a target patch basing on the “lattice” (or reseau or array) layout³⁵ shown in Fig. 4. Particularly, there exists one additional layer in the patch-level side, namely the Layer IV+, where we give weights w_m to the obtained three patch-unary potentials, respectively. To obtain the optimal combination of w_m , we iteratively calculate the three potentials to get the best patch-unary segmentation result. Similarly, we give weights $w_{(m,n)}$ to three patch-binary potentials to obtain an optimal patch-binary segmentation result.
- In Layer V, first, we give weights w_V and w_E to two obtained pixel-level potentials (pixel-unary and pixel-binary potentials), respectively; and give weights w_{VP} and w_{EP} to two obtained patch-level potentials (patch-unary and patch-binary potentials), respectively. Then,

we calculate the joint probability of these four potentials to structure the final HCRF model.

- In Layer VI, in order to further improve the segmentation result from Layer V, we use MRF and morphological operations as post-processing in our work.

3.2.2 Pixel-unary Potential

The pixel-unary potential $\varphi_i(x_i; \mathbf{Y}; w_V)$ in Eq. (3) is related to the probability weights w_V of a label x_i , taking a value $c \in \mathbb{L}$ given the observation data Y by Eq. (5).

$$\varphi_i(x_i; \mathbf{Y}; w_V) \propto \left(p(x_i = c | f_i(Y)) \right)^{w_V}, \quad (5)$$

where the image content is characterized by site-wise feature vector $f_i(Y)$ which may be determined by all the observation data Y .⁴⁹ The observation depicts a pixel whether belongs to a gastric cancer region or to the background. Especially, considering the effectiveness of U-Net in medical image segmentation tasks, for $f_i(Y)$, we use $256 \times 256 \times 2$ -dimensional pixel-level feature F_i , obtaining feature maps at the penultimate convolution layer of the U-Net and the probability maps $p(x_i = c | f_i(Y))$ at the last convolution layer of the U-Net.³⁶ So, the pixel-unary potential is updated to Eq. (6).

$$\varphi_i(x_i; \mathbf{Y}; w_V) = \varphi_i(x_i; F_i; w_V), \quad (6)$$

where the data Y determines F_i .

3.2.3 Pixel-binary Potential

The pixel-binary potential $\psi_{(i,j)}(x_i, x_j; \mathbf{Y}; w_E)$ in Eq. (3) conveys how similarly the pairwise adjacent sites i and j is to take label $(x_i, x_j) = (c, c')$ given the data⁴⁹ and weights, and it is defined as

Eq. (7).

$$\psi_{(i,j)}(x_i, x_j; \mathbf{Y}; w_E) \propto \left(p(x_i = c; x_j = c' | f_i(Y), f_j(Y)) \right)^{w_E}. \quad (7)$$

The layout of the pixel-binary potential is shown in Fig. 3. This “lattice” (or reseau or array) layout is used to describe the probability of each classified pixel by averaging each pixel of neighbourhood unary probability.³⁵ The other procedures are identical to the pixel-unary potential calculation in Sec. 3.2.2.

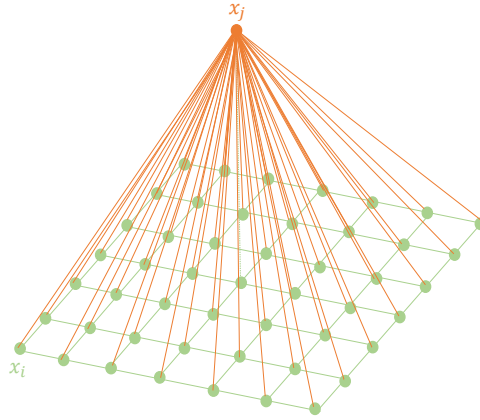


Fig 3 48 neighbourhood “lattice” (or reseau or array) layout of the pixel-binary potential. The average of the unary probabilities of the 48 neighbourhood pixels is used as the probability of the pixel (the central pixel in orange).

3.2.4 Patch-unary Potential

In order to extract abundant spatial information, we choose VGG-16, Inception-V3 and ResNet-50 networks to extract patch-level features. In patch-level terms, we use α, β, γ to represent VGG-16, Inception-V3 and ResNet-50 networks, respectively. In patch-unary potentials $\varphi_m(x_m; \mathbf{Y}; w_m; w_{VP})$ of Eq. (3), label $x_m = \{x_{(m,\alpha)}, x_{(m,\beta)}, x_{(m,\gamma)}\}$ and $w_m = \{w_{(m,\alpha)}, w_{(m,\beta)}, w_{(m,\gamma)}\}$. $\varphi_m(x_m; \mathbf{Y}; w_m; w_{VP})$ are related to the probability of labels $(w_{(m,\alpha)}, w_{(m,\beta)}, w_{(m,\gamma)}) = (c, c, c)$ given the data Y by

Eq. (8).

$$\begin{aligned} \varphi_m(\mathbf{x}_m; \mathbf{Y}; w_m; w_{V_P}) &\propto \left((p(\mathbf{x}_{(m,\alpha)} = c | f_{(m,\alpha)}(Y)))^{w_{(m,\alpha)}} \right. \\ &\left. (p(\mathbf{x}_{(m,\beta)} = c | f_{(m,\beta)}(Y)))^{w_{(m,\beta)}} (p(\mathbf{x}_{(m,\gamma)} = c | f_{(m,\gamma)}(Y)))^{w_{(m,\gamma)}} \right)^{w_{V_P}}, \end{aligned} \quad (8)$$

where the characteristics in image data are transformed by site-wise feature vectors $f_{(m,\alpha)}(Y)$, $f_{(m,\beta)}(Y)$ and $f_{(m,\gamma)}(Y)$ that may be determined by all the input data Y . For $f_{(m,\alpha)}(Y)$, $f_{(m,\beta)}(Y)$, and $f_{(m,\gamma)}(Y)$, we use 1024-dimensional patch-level bottleneck features $F_{(m,\alpha)}$, $F_{(m,\beta)}$ and $F_{(m,\gamma)}$, obtained from pre-trained VGG-16, Inception-V3 and ResNet-50 by ImageNet; and retrain their last three fully connected layers⁵⁰ using gastric histopathology images to obtain the classification probability of each class. So, the patch-unary potential is updated to Eq. (9).

$$\varphi_m(\mathbf{x}_m; \mathbf{Y}; w_m; w_{V_P}) = \varphi_m(\mathbf{x}_m; F_{(m,\alpha)}; F_{(m,\beta)}; F_{(m,\gamma)}; w_m; w_{V_P}), \quad (9)$$

where the data Y determines $F_{(m,\alpha)}$, $F_{(m,\beta)}$ and $F_{(m,\gamma)}$.

3.2.5 Patch-binary potential functions

The patch-binary potential $\psi_{(m,n)}(\mathbf{x}_m, \mathbf{x}_n; \mathbf{Y}; w_{(m,n)}; w_{E_P})$ of the Eq. (3) denotes how similarly the pairwise adjacent patch sites m and n is to take label $(\mathbf{x}_m, \mathbf{x}_n) = (c, c')$ given the data and weights, and it is defined as Eq. (10).

$$\begin{aligned} \psi_{(m,n)}(\mathbf{x}_m, \mathbf{x}_n; \mathbf{Y}; w_{(m,n)}; w_{E_P}) &\propto \\ &\left((p(\mathbf{x}_{(m,\alpha)} = c; \mathbf{x}_{(n,\alpha)} = c' | f_{(m,\alpha)}(Y), f_{(n,\alpha)}(Y)))^{w_{(m,n,\alpha)}} \right. \\ &(p(\mathbf{x}_{(m,\beta)} = c; \mathbf{x}_{(n,\beta)} = c' | f_{(m,\beta)}(Y), f_{(n,\beta)}(Y)))^{w_{(m,n,\beta)}} \\ &\left. (p(\mathbf{x}_{(m,\gamma)} = c; \mathbf{x}_{(n,\gamma)} = c' | f_{(m,\gamma)}(Y), f_{(n,\gamma)}(Y)))^{w_{(m,n,\gamma)}} \right)^{w_{E_P}}, \end{aligned} \quad (10)$$

where $x_n = \{x_{(n,\alpha)}, x_{(n,\beta)}, x_{(n,\gamma)}\}$ denotes the patch labels and $w_{(m,n)} = \{w_{(m,n,\alpha)}, w_{(m,n,\beta)}, w_{(m,n,\gamma)}\}$ represents the patch weights. A “lattice” (or reseau or array) layout in Fig. 4 is designed to calculate the probability of each classified patch by averaging each patch of neighbourhood unary probability.³⁵ The other operations are similar to the patch-binary potential in Sec. 3.2.4.

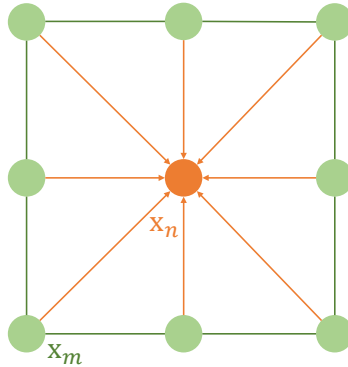


Fig 4 Eight neighbourhood “lattice” (or reseau or array) layout of the patch-binary potential. The average of unary probabilities of the eight neighbourhood patches is utilized as the probability of the central target patch.

4 Results

4.1 Experimental Settings

4.1.1 Dataset

In this research, we utilize a publicly accessible H&E stained gastric histopathological image dataset in $20\times$ magnification,⁵¹ as represented in Fig. 5. In this dataset, the image format is “*.tiff” or “*.png” and practical histopathologists mark most of the abnormal regions in histopathology images of gastric cancer. The dataset consists of 140 normal images without GT images, and 560 abnormal images with 560 GT images where the positive regions (cancerous cells) are labelled. There exists no positive regions in the normal images and positive regions appear in the abnormal images. The size of the gastric histopathological image is 2048×2048 pixels.

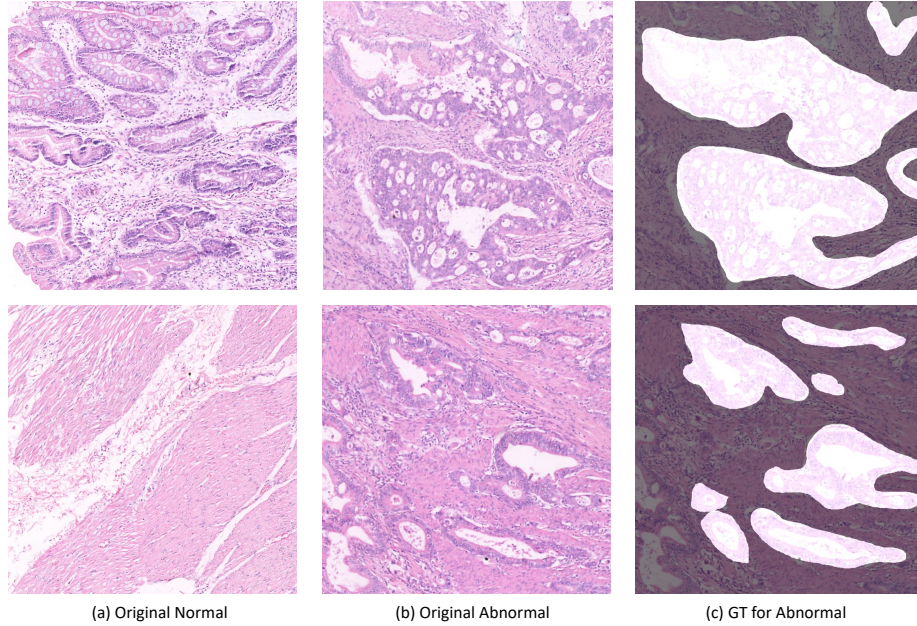


Fig 5 Examples in the H&E stained gastric histopathological image dataset. The column (a) presents the original images of normal tissues. The original images in column (b) contain abnormal regions, and column (c) shows the corresponding GT images of the abnormal regions. In the GT images, the brighter regions are positive (abnormal tissues with cancer cells), and the darker regions are negative (normal tissues without cancer cells).

4.1.2 Training, Validation and Test Data Setting

In the GHIS task, we only use the 560 abnormal images and their corresponding GT images from the gastric histopathological image dataset. The abnormal images in the dataset are partitioned into training, validation and test sets randomly at ratio 1:1:2. The dataset setting is represented in Table 1.

Table 1 Distribution of data for training, validation and testing.

Image type	Training	Validation	Test	Sum
Original images	140	140	280	560

In the pixel-level potentials, we flip the original and GT images horizontally and vertically and rotate them 90, 180, 270 degrees to augment the training and validation datasets 6 times. Furthermore, because the size of the gastric histopathology images is too large to process, we crop the original and the GT images into 256×256 pixels. The data augmentation for the pixel-level

training is shown in Table 2.

Table 2 Data augmentation for training and validation sets in pixel-level training. Image types are presented in the first column. The usages of data are shown in the second and third columns. The total number of images used in this paper is presented in last column.

Image type	Training	Validation	Sum
Original images	140	140	280
Augmented images	53760	53760	107520

In the patch-level potential, we mesh the original and GT images into patches (64×64 pixels) and the area of a patch is 4096 pixels. When the sum of the pixel numbers in a GT image is over 2048, we give a positive label (1, foreground) to the corresponding original image patch; otherwise, we give it a negative label (0, background). However, when we do this operation, the positive image patches are much less than the negative image patches. So, in order to balance the data during training, we augment the positive image patches by flipping horizontally and vertically and rotating them to 90, 180, 270 degrees in the training set. Meantime, we do the same augmentation to the images in the validation set. The data augmentation for the patch-level is shown in Table 3.

Table 3 Data augmentation for training and validation sets in patch-level training. Image types are presented in the first column. The different usages of data are shown in the second and third columns. The bottom row presents the total number of images used in this paper.

Image type	Train	Validation
Augmented positive images	121251	119151
Augmented negative images	121251	119151
Sum	242502	238302

4.2 Evaluation of Pixel-level Potentials

4.2.1 Evaluation Criteria

First, we use the training and validation sets in Table 2 to train the U-Net. The validation set is applied to tune the CNN parameters and avoid the CNN overfitting or underfitting during the training

process. Second, we obtain the prediction probability of each pixel in an image in validation and test sets. Thirdly, in order to evaluate the segmentation performance, we split joint the 256×256 pixel images to 2048×2048 pixel images, and use 140 validation images of 2048×2048 pixels and 280 test images of 2048×2048 pixels to evaluate the segmentation result. To give a quantitative evaluation, we use Sørensen-Dice coefficient (Dice or F1-score), relative volume difference (RVD), intersection over union (IoU or Jaccard), precision (or positive predictive value), recall (or sensitivity), specificity (or true negative rate) and accuracy to measure the segmentation result, where these criteria are common and suitable for medical image segmentation evaluation.⁵²⁻⁵⁵

These seven criteria are defined in Table 4.

Table 4 The seven evaluation criteria and corresponding definitions.

Criterion	Definition	Criterion	Definition
Dice	$\frac{2TP}{2TP + FP + FN}$	Recall	$\frac{TP}{TP + FN}$
RVD	$ \frac{FP + TP}{TP + FN} - 1$	Specificity	$\frac{TN}{TN + FP}$
IoU	$\frac{TP}{TP + FN + FP}$	Accuracy	$\frac{TP + TN}{TP + FN + TN + FP}$
Precision	$\frac{TP}{TP + FP}$		

In the definition of these criteria, TP denotes the true positive, which are positive cases diagnosed as positive. TN denotes the true negative, which are negative cases diagnosed as negative. FP denotes the false positive, which are negative cases diagnosed as positive. and FN denotes the false negative, which are positive cases diagnosed as negative. Dice is in the interval $[0,1]$, and a perfect segmentation yields a Dice of 1. RVD is an asymmetric metric, and a lower RVD means a better segmentation result.⁵⁵ IoU is a standard metric for segmentation purposes that computes a ratio between the intersection and the union of two sets, and a high IoU means a better seg-

mentation result.⁵² Precision is utilized to measure the proportion of the relevant cases among the retrieved cases, where a higher precision implies a method obtains more relevant cases than irrelevant results substantially. Recall is used to estimate the proportion of relevant cases which have been retrieved in the total number of relevant cases, where if a method obtains most of the relevant cases, it gets a high recall. Specificity is a metric of the ratio of actual negative cases which are correctly distinguished.⁵⁶ Segmentation accuracy is the correct predicted pixels among the whole pixels, where a high accuracy means a better segmentation result.

4.2.2 Evaluation for Pixel-level Segmentation Results

From Fig. 6, we can see examples of the segmentation results on the validation set, where we use different colors to describe different predicted probabilities. The probabilities are the higher, the regions have a greater risk to contain cancer tissues inside. The black, yellow, orange, tomato, red and purple colors represent the probabilities between $[0, 0.5)$, $[0.5, 0.6)$, $[0.6, 0.7)$, $[0.7, 0.8)$, $[0.8, 0.9)$ and $[0.9, 1]$, respectively.

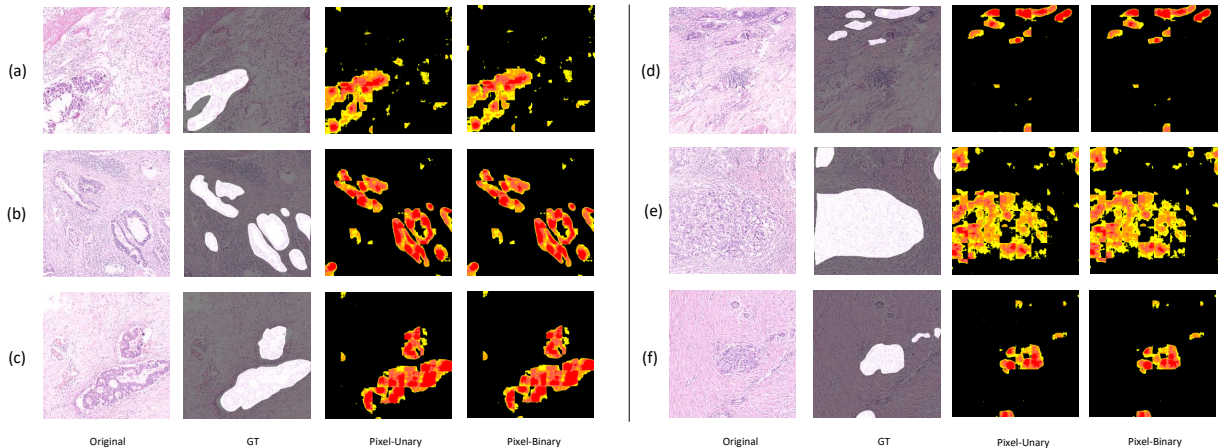


Fig 6 Examples of the pixel-level segmentation results on the validation set. The original and their GT images is respectively presented in the first and second columns. The third and last columns are the image segmentation results with pixel-unary and pixel-binary potentials, respectively. (a) is an image with a single abnormal region. (b) and (c) are examples for multiple abnormal regions. (d) represents the case with very small abnormal regions. (e) is an example with a very big abnormal region. (f) shows an un conspicuous case of abnormal regions.

The original images in Fig. 6 are common and representative cases in our GHIS work, so we choose them as visible comparison in this paper. We can find that the pixel-binary potential results remove some noise that appears in the pixel-unary potential results, showing a stronger denoising ability. However, because the binary-pixel potential makes some correctly classified pixel in the pixel-unary potential go wrong, the pixel-unary potential still makes sense in our HCRF model with a complementarity to the pixel-binary potential. Meanwhile, the evaluation indexes are show in Fig. 7.

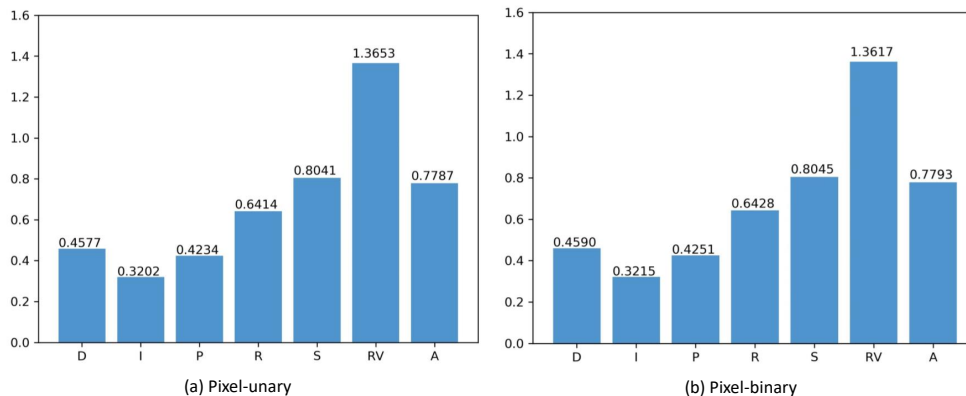


Fig 7 The evaluation for the image segmentation performance of the pixel-level potentials on the validation set. (a) and (b) are the evaluations of pixel-unary and pixel-binary potentials on the validation set, respectively. D, I, P, R, S, RV and A represent Dice, IoU, precision, recall, specificity, RVD and accuracy, respectively.

4.3 Evaluation of Patch-Level Potentials

4.3.1 Evaluation for Patch-level Segmentation Results

First, we train the VGG-16, Inception-V3 and ResNet-50 networks separately, using the training and validation sets in Table 3. Then, we get the label and predicted probability of each image patch. The classification accuracy of 238302 image patches in the validation set is shown in Table 5.

From Table 5, we can figure out the VGG-16 performs well both in the patch-unary and -binary potentials, showing a strong feature extraction ability of this network model in the histopathology

Table 5 Classification accuracies of three CNNs on the validation set in patch-level training. The first column shows the different patch-level potentials. The second to the last columns show different CNNs.

Potentials	VGG-16	Inception-V3	ResNet-50
Patch-unary	0.7226	0.6889	0.7118
Patch-binary	0.7331	0.7139	0.7494

image analysis work. Further more, the classification confusion matrices are shown in Fig. 8.



Fig 8 Image patch classification results of three CNNs on the validation set. The confusion matrices in the left, middle and right columns present the classification results of VGG-16, Inception-V3 and ResNet-50 networks of patch-unary and -binary potentials, respectively, where 1 represents positive and 0 represents negative.

Furthermore, in order to visualize the classification results, we piece together the patches and obtain the patch-level segmentation results, including three patch-unary results and three patch-binary results in Fig. 9. The probabilities of image patches corresponding to colors are set as the same as the pixel-level potentials in Sec. 4.2.2.

From Fig. 9, we can find that the patch-binary segmentation can eliminate the noise vary effectively. However, it may change some correctly segmented regions in the patch-unary potential to wrong segmentation results. So, both the patch-unary and patch-binary potentials make sense in

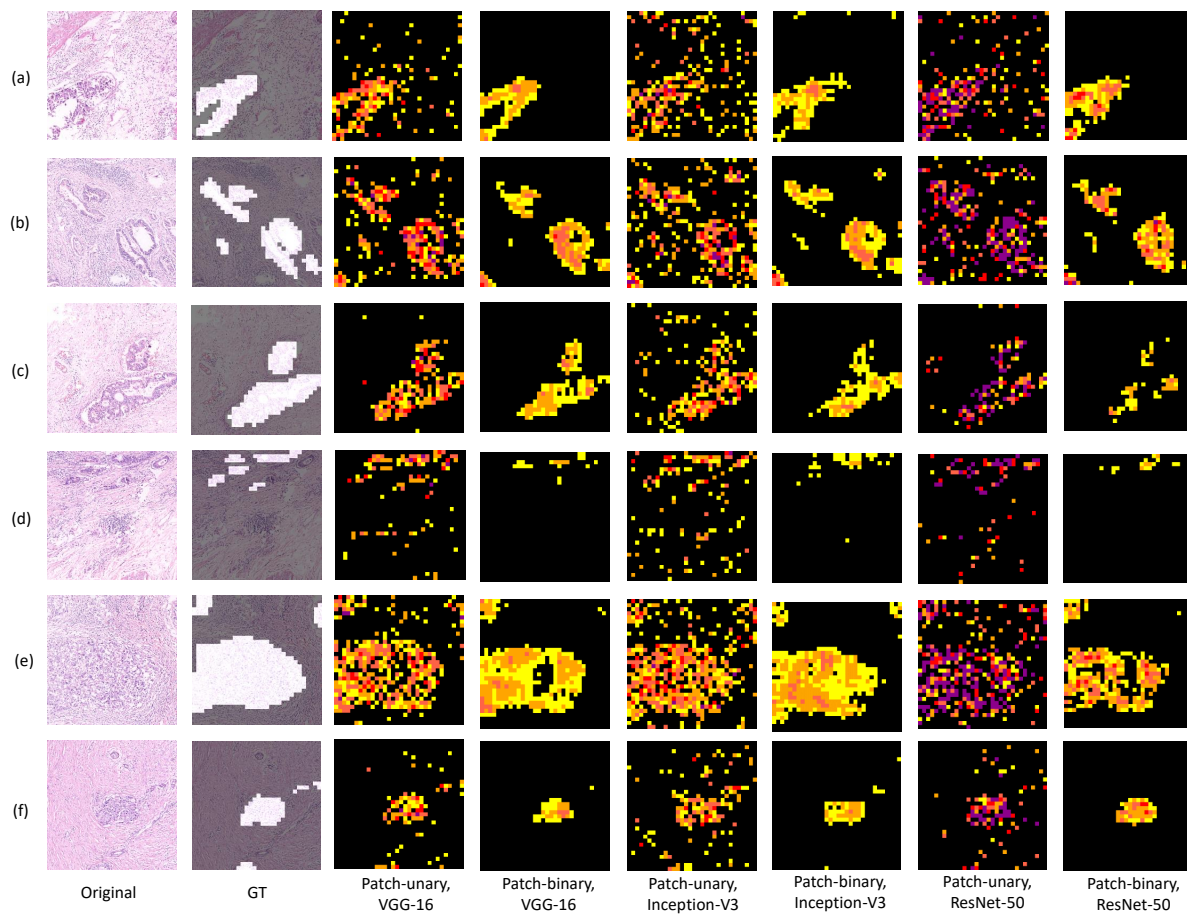


Fig 9 Examples of the patch-level segmentation results of three CNNs on the validation set. The first and second columns show the original and their GT images. The third and fourth columns are the VGG-16 results, the fifth and sixth columns are the Inception-V3 results and the seventh and last columns are the ResNet-50 results.

our HCRF model.

4.3.2 Optimization for Patch-unary and -binary Potentials

In order to further optimize the patch-unary and -binary segmentation results, we combine three patch-unary potentials and three patch-binary potentials to obtain one patch-unary potential and one patch-binary potential, respectively. Here, two optimization strategies are compared: The first is a direct “late fusion” strategy,⁵⁷ where the classification probabilities of the VGG-16, Inception-V3 and ResNet-50 networks are given weights with a 1:1:1 ratio and summed together to obtain a joint classification probability. The second is a grid optimization strategy,⁵⁸ where, based on our pre-tests, a step length of 0.05 is applied to give independent weights to the classification probabilities of the VGG-16, Inception-V3 and ResNet-50 networks. Additionally, in order to guarantee the image patch classification accuracy, we carry out the log operation to the probability. When we calculate the joint probability, this operation leads to a nonlinear case. So, in the optimized patch-level image segmentation results, we only use one pinkish-orange color to represent the positive regions and another black color to represent the negative regions.

Optimization for Patch-unary Potentials: For the patch-unary potentials, the weights by the grid optimization is shown in Table 6.

Table 6 The patch-unary weights of three CNNs using the grid optimization. The first row presents the CNNs. The second row presents the CNN weights.

CNN	VGG-16	Inception-V3	ResNet-50
Weight	0.55	0.25	0.20

From Table 6, we can figure out that, due to the VGG-16 network has a better image segmentation performance than that of other CNNs involved, it obtains the highest weight of 0.55. However, although the Inception-V3 and ResNet-50 networks have a weaker performance than the VGG-16,

they still contribute to the final segmentation results, so they share the remaining weights with 0.25 and 0.20. Furthermore, examples of the optimized patch-unary segmentation results are shown in Fig. 10.

In Fig. 10, the grid optimization approach achieves a better image segmentation performance in details of the cancer regions. For more details, we give a comparison with the image patch classification confusion matrices in Fig. 11.

From Fig. 11, we can figure out the grid optimization achieves a higher classification accuracy than that of the direct late fusion approach on both the foreground (0.7560) and background (0.7348) patches, as well it obtains a higher overall accuracy (0.7450) for all patches.

Optimization for Patch-binary Potentials: For the patch-binary potentials, the weights by the grid optimization is shown in Table 7.

Table 7 The patch-binary weights of three CNNs using the grid optimization. The first row presents the CNNs. The second row presents the weights.

CNN	VGG-16	Inception-V3	ResNet-50
Weight	0.40	0.00	0.60

From Table 7, we can find that, due to the ResNet-50 and VGG-16 networks have more robust image segmentation performance than that of the Inception-V3 network, they obtain 0.60 and 0.40 weights, respectively. However, because the Inception-V3 network has a much worse performance and it does not contribute any information to the final segmentation results, it is assigned a 0 weight. In addition, examples of the optimized patch-binary segmentation results are shown in Fig. 10.

In Fig. 10, the grid optimization strategy obtains a more clean image segmentation result, where more noise outside the cancer regions is removed. A comparison with the image patch classification confusion matrices is given in Fig. 11.

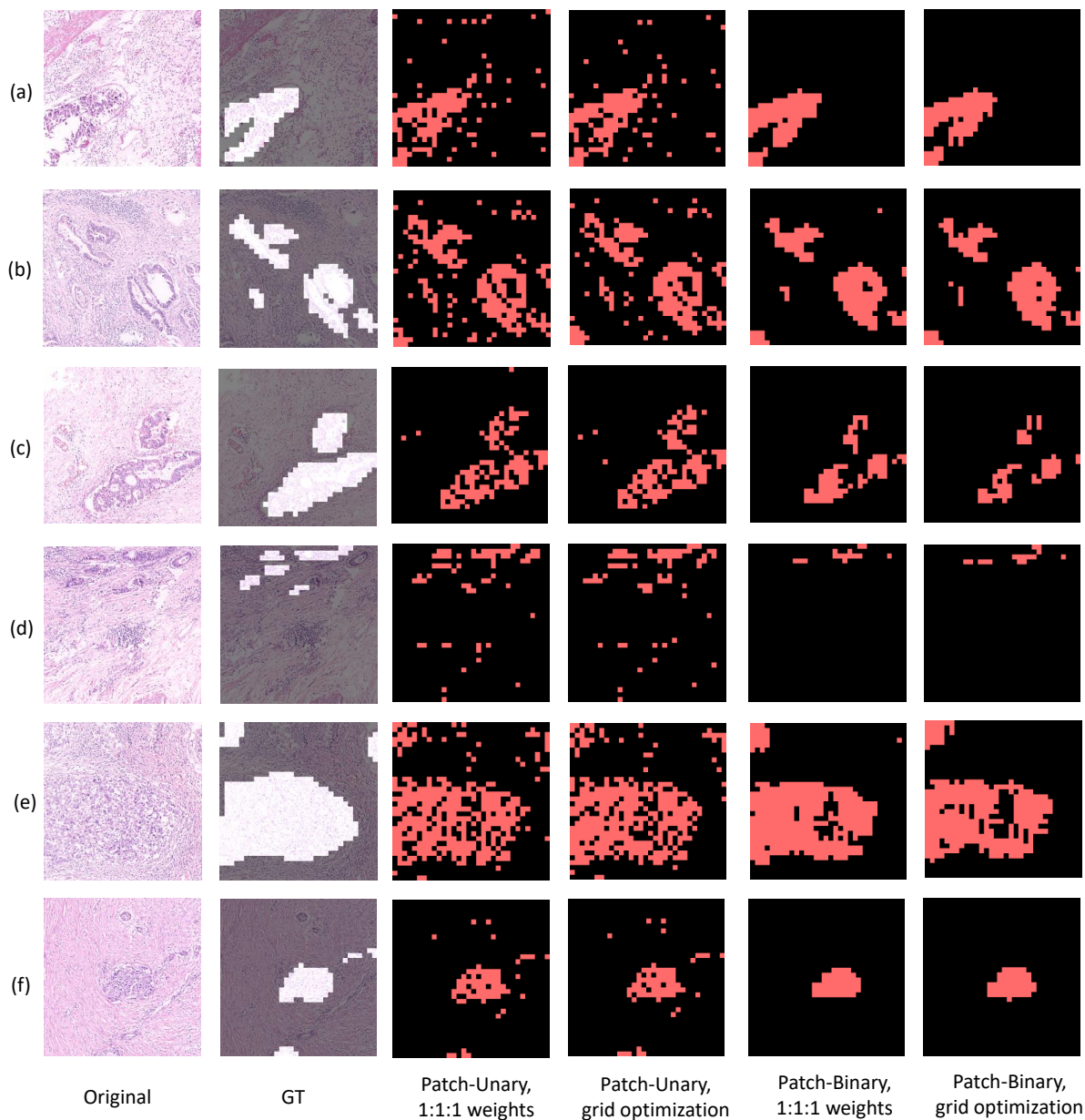


Fig 10 Examples of the optimized patch-unary and patch-binary segmentation results on the validation set. The first and second columns present the original and their GT images, respectively. The third and forth columns are the optimized patch-unary image segmentation results. In the third column, VGG-16, Inception-V3 and ResNet-50 networks have their patch-unary weights with a 1:1:1 ratio. In the forth column, these three CNNs have their weights as shown in Table 6. The fifth and last columns are the optimized patch-binary image segmentation results. In the fifth column, VGG-16, Inception-V3 and ResNet-50 networks have their weights with a 1:1:1 ratio. In the last column, these three CNNs have their weights as shown in Table 7.

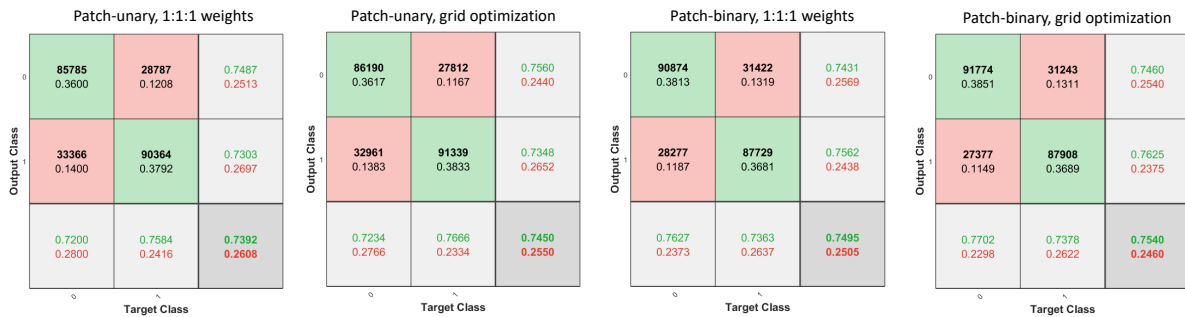


Fig 11 Image patch classification results of the optimized patch-unary and patch-binary potentials on the validation set. The first and second confusion matrices correspond to the 1:1:1 weighting and the grid optimization results of patch-unary potentials, respectively. The third and last confusion matrices correspond to the 1:1:1 weighting and the grid optimization results of patch-binary potentials, respectively. 1 represents positive and 0 represents negative.

From Fig. 11, we can figure out the grid optimization for patch-binary potentials obtains a higher classification accuracy than that of the direct late fusion approach on the foreground (0.7460), background (0.7625) and all (0.7540) image patches.

4.4 Evaluation of the Proposed HCRF Model

4.4.1 Evaluation of the HCRF and Post-processing

Based on the pixel-level and patch-level image segmentation results in Sec. 4.2 and 4.3, the final result by the HCRF model is obtained, where we use the pixel-unary, pixel-binary, patch-unary and patch-binary segmentation accuracies as the weights to optimize the HCRF model. Specifically, because all of these four accuracies (0.7787, 0.7793, 0.7450 and 0.7540) are in $[0.7, 0.8]$ and lack of discrimination, and considering the computation efficiency of 2048×2048 pixels, we use them to minus 0.7 to enhance their distinction. Hence, we have the weights of 0.087, 0.0793, 0.0450 and 0.0540 for pixel-unary, pixel-binary, patch-unary and patch-binary potentials, respectively. In addition, the segmentation result with the post-processing is also achieved. Examples of the HCRF segmentation results are shown in Fig. 12.

From Fig. 12, we can find that the HCRF model achieves better image segmentation perfor-

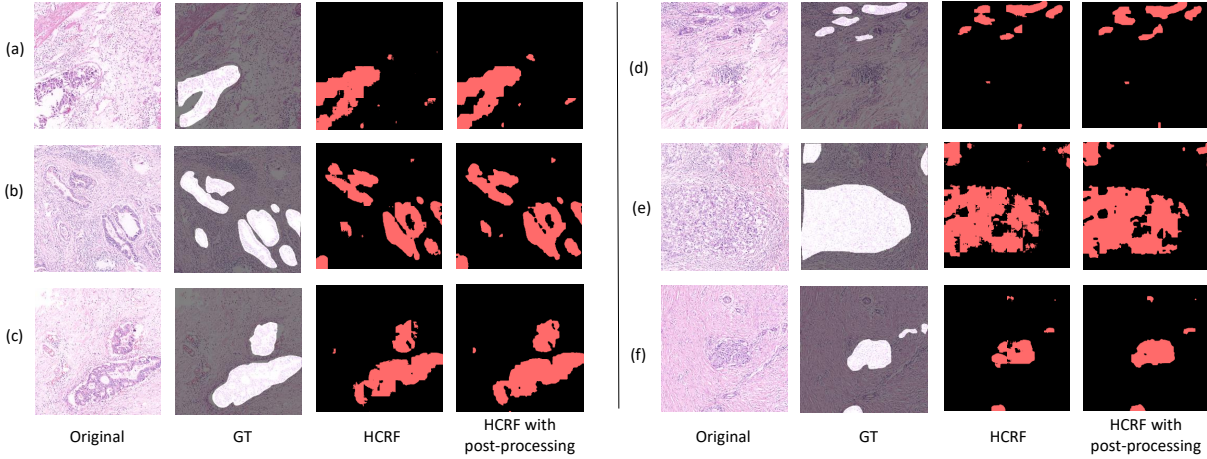


Fig 12 Examples of the HCRF image segmentation results on the validation set. The first and second columns present the original and their GT images, separately. The HCRF image segmentation results and that with the post-processing are shown in the third and last columns.

mance than that of the pixel-level potentials in Fig. 6, where the over-segmentation and under-segmentation cases are reduced. Specially, when the post-processing consisted of two steps which are MRF and morphological operation including once open operation is applied, the segmentation performance is further improved. In addition, the numerical evaluation for the HCRF segmentation performance is shown in Fig. 13.

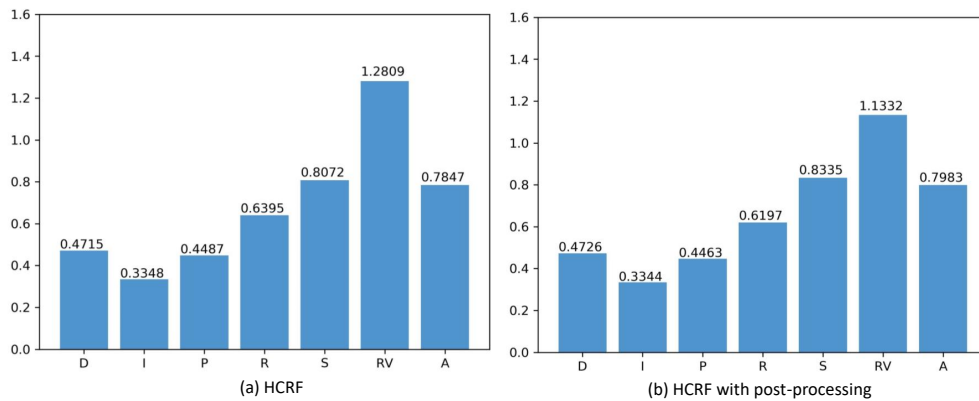


Fig 13 The evaluation for the image segmentation performance of the proposed HCRF model on the validation set. (a) and (b) are the evaluations of the proposed HCRF model and that with the post-processing on the validation set, respectively.

From the comparison for seven evaluation criteria of the HCRF and HCRF with post-processing in Fig. 13, we can find that, four of them are improved (Dice, specificity, RVD and accuracy)

and two of them are at nearly the same level (IoU and precision). Hence, the HCRF with post-processing has as an overall improved image segmentation performance, and we choose it in our following experimental steps.

4.4.2 Evaluation of the HCRF Model on the Test Set

In order to prove the effectiveness of the proposed HCRF model (with the post-processing), we examine it on the test set, and examples of the segmentation results, which include small and large targets, are presented in Fig. 14.

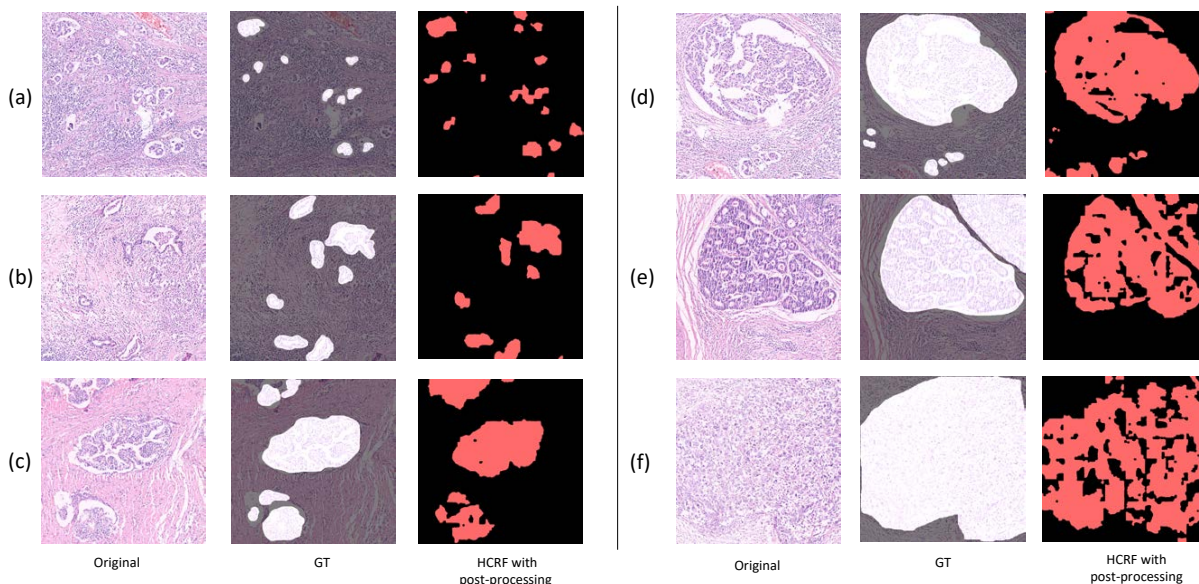


Fig 14 Examples of the HCRF segmentation results on the test set. The first and middle columns present the original and GT images in the test set, separately. The last column shows the image segmentation results by the proposed HCRF model (with the post-processing). (a) to (f) are six examples.

From Fig. 14, we can discover our HCRF model obtains good image segmentation results on the test set, where most of the positive (cancer) regions are segmented, and the edges of the regions are smooth. Furthermore, a numerical evaluation for the HCRF segmentation performance on the test set is compared with that on the validation set in Fig. 15.

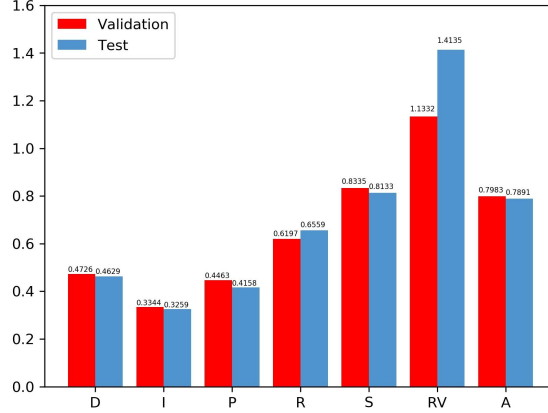


Fig 15 A comparison between the image segmentation performance of the HCRF model with post-processing on the validation and test sets.

The comparison in Fig. 15 reveals that although the test set has 280 images which are twice than the validation set, our proposed HCRF model also obtains good segmentation performance, where the values of all seven evaluation indexes on the test set are closed to that on the validation set, showing a high stability and a strong robustness of our method.

4.5 Comparison to Existing Methods

4.5.1 Existing Methods

In order to show the potential of the proposed HCRF method for the GHIS task, we compare it with seven existing methods, including three state-of-the-art methods (DenseCRF,⁶ SegNet⁵⁹ and U-Net) and four classical methods (Otsu thresholding,⁶⁰ Watershed,⁶¹ k -means clustering⁶² and MRF). The experimental settings of these existing methods are briefly introduced as follows:

- (1) The DenseCRF bases on U-Net features which is trained on the dataset in Table 2 and gets 2048×2048 images finally.
- (2) The U-Net is retrained on the dataset in Table 2 and gets 2048×2048 images finally.
- (3) The SegNet is retrained on the dataset in Table 2 and gets 2048×2048 images finally.
- (4) The Otsu thresholding method is used on the dataset in Table 1.
- (5) The Watershed algorithm is used with a two-stage way, where it is applied twice on the dataset in Table 1.
- (6) The

k -means method is trained on the dataset in Table 1. (7) The MRF segmentation method is applied to the dataset in Table 1 and it includes two steps. First, we use k -means for clustering, then we use the MRF to the k -means result.

4.5.2 Image Segmentation Result Comparison

Fig. 16 shows an example of the segmentation results of our method and seven existing methods on the test set in Table 1.

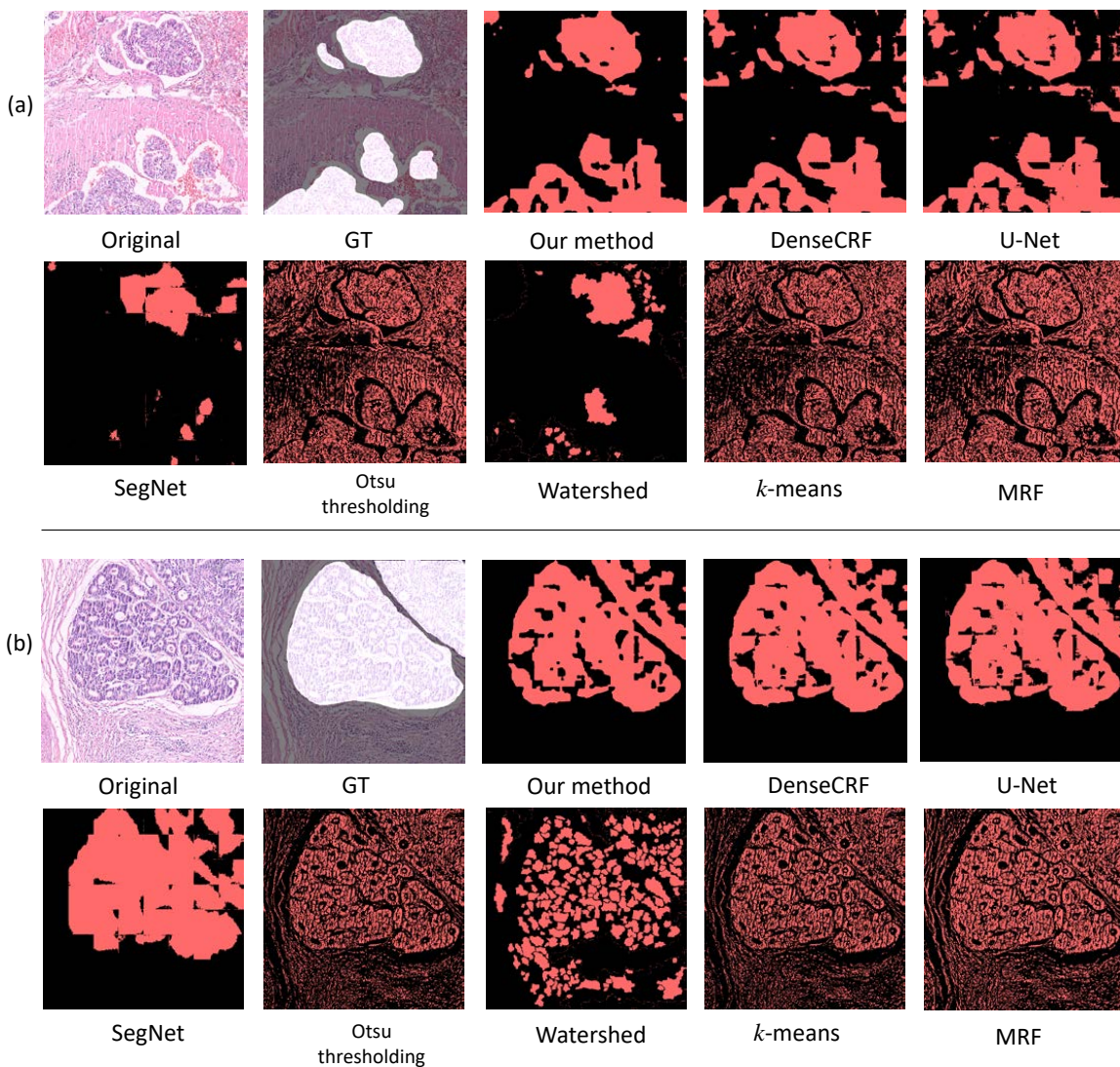


Fig 16 A comparison of the image segmentation results of our HCRF and other existing methods on the test set.

From Fig. 16, we can find our HCRF method has a better image segmentation performance

than other existing methods in the visible comparison, where more positive regions (cancer) are correctly marked and less noise is remained. Furthermore, a numerical comparison between our HCRF method and other existing methods on the test set is given in Table 8.

Table 8 A numerical comparison of the image segmentation performance between our HCRF model and other existing methods. The first row shows different methods. The first column shows the evaluation criteria. The bold texts are the best performance for each criterion.

Criterion	Our HCRF	DenseCRF	U-Net	SegNet	Otsu thresholding	Watershed	<i>k</i> -means	MRF
Dice	0.4629	0.4578	0.4557	0.2008	0.2534	0.2613	0.2534	0.2396
IoU	0.3259	0.3212	0.3191	0.1300	0.1505	0.1585	0.1506	0.1432
Precision	0.4158	0.4047	0.4004	0.3885	0.2159	0.2930	0.2165	0.1839
Recall	0.6559	0.6889	0.6896	0.3171	0.4277	0.3541	0.4284	0.4991
Specificity	0.8133	0.7812	0.7795	0.8412	0.7082	0.7942	0.7078	0.5336
RVD	1.4135	1.6487	1.6736	2.0660	2.8859	1.9434	2.8953	4.5878
Accuracy	0.7891	0.7702	0.7684	0.7531	0.6598	0.7205	0.6593	0.5441

Table 8 indicates that: (1) Comparing to the state-of-the-art methods (DenseCRF, U-Net and SegNet), except recall and specificity, our HCRF behaves all better on other indexes. The precision has more effectiveness to evaluate the foreground segmentation result and recall has more effectiveness to evaluate the background segmentation result. When we focus on optimizing the foreground (the positive or abnormal regions), we get lower FP and higher precision. Meantime the recall is opposite to precision. However, the Dice is a balance between the precision and recall, and our HCRF obtains the highest Dice value, showing an overall better image segmentation performance. Form Fig. 16, we can find out that the SegNet may classify some abnormal areas to normal which leads to high TN, meantime, high specificity. (2) Comparing to classical methods (Otsu thresholding, Watershed, *k*-means clustering and MRF), our HCRF model has better segmentation results. These classical methods have similar results, where they cannot separate entire abnormal areas, but get more unnecessary details in both normal and abnormal areas.

4.6 Computational Time

At last, the computational time of our HCRF model is concisely depicted. A workstation equipped with Intel® Core™ i7-8700k CPU with 3.20GHz, GeForce RTX 2080 with 8GB and 32GB RAM is utilized in the experiment. When we retrain the U-Net and fine-tune the VGG-16, Inception-V3 and ResNet-50 networks, we use Keras framework fore-end and Tensorflow framework back-end. Table 9 shows the retraining time of the U-Net and fine-tuning time of the VGG-16, Inception-V3 and ResNet-50 networks.

Table 9 The training time of four CNNs using 140 training and 140 validation images.

CNN	U-Net	VGG-16	Inception-V3	ResNet-50
Time/hours	37.7	10.0	6.1	5.6

Furthermore, Table 10 shows the testing time of our HCRF model on 280 images (2048×2048 pixels) within two working stages. The first stage is the “Main Body” of the HCRF model, which is the stage from Layer I to Layer V in Fig. 2. The second stage is the “Post-processing” stage, which denotes Layer VI in Fig. 2. For histopathologists in the practical work, if they want a faster segmentation result, they can just run the Main Body stage of our HCRF model; if they want a more accurate segmentation result, they can run the whole HCRF model with the post-processing stage.

Table 10 The testing time of our HCRF on 280 gastric histopathology images.

Time	Main Body	Post-Processing	Sum
Total Time/hours	2.2	2.7	4.9
Mean Time/seconds	28.1	33.5	61.6

5 Discussion

5.1 Comparison between the Proposed HCRF Model and Previous Studies

Although our HCRF model achieves good gastric histopathology image segmentation performance, we compare our method to the previous GHIS studies in Table 11. We choose a regularly used and effective criterion that is segmentation accuracy as the comparison metric. With the advancement of the machine vision algorithm applied in the pathology image segmentation and hardware computing power, the segmentation task in gastric histopathology image turns to tissue-scale from cell-scale.³ The tissue-scale segmentation task is more difficult, because the tissue-scale content is more complex than the cell-scale content which only includes nuclei and cytoplasm. We can find that cell-scale segmentation task usually need less images,^{16,17} because one gastric cancer slice includes massive separated cells for training. The most popular algorithm applied in the tissue-scale gastric is FCN^{18,21} and some which involve addition of modules to FCN,^{19,20,22} generally, they obtain high segmentation accuracies. Training the FCN for tissue-scale segmentation usually need a well-labelled dataset,^{19,20,22} for our dataset which is weakly labelled, we do not concentrate on optimizing the FCN structures, instead, we just embed the U-Net to our proposed HCRF model for extracting pixel-level features and aiming to extract more higher order information to characterize the gastric histopathology image and we achieve high segmentation accuracy as well. In Table 11, we can discover that the segmentation time for one gastric slice ranging from 5.1 seconds to 244 seconds and our computational time is in the middle level. However, the computational power of different methods are hard to measure for the different image size and equipment.

Despite we use a publicly accessible gastric histopathology image dataset, there exists barriers to compare our studies to previous studies. The datasets used in^{18,19} are identical with ours.

Table 11 A comparison of the image segmentation methods in gastric histopathology studies

Method	Segmentation scale	Training	Validation	Test	Accuracy	Time per slice/seconds
MM ¹⁵	Cell	-	-	35	-	72.5 ± 18.2
CNN3 ¹⁶	Cell	12	4	14	-	30
NBN ¹⁷	Cell	12	4	14	-	5.1
SWB (AlexNet) ¹⁸	Tissue	300	-	100	0.821	244.3
FCN (AlexNet) ¹⁸	Tissue	300	-	100	0.657	12.5
FCN (GoogLeNet) ¹⁸	Tissue	300	-	100	0.785	14.8
GT-Net ¹⁹	Tissue	560	-	112	-	-
RMDL ²⁰	Tissue	408	-	200	0.865	93.79
RL ²¹	Tissue	1400	400	100	0.9145	11
DCMEN ²²	Tissue	350	-	150	0.916	-
HCRF (our method)	Tissue	280	140	140	0.7891	61.6

However, they only use a part of the dataset for training and testing in.¹⁸ Though we use less training data and more abnormal images in test dataset to verify our segmentation model, we achieve similar segmentation performance with the SWB (AlexNet) and FCN (GoogLeNet) in.¹⁸ Because the different abnormal images, which are randomly selected, are used in the test dataset, there exists bias in segmentation result evaluation. Since the abnormal areas in the gastric histopathology images of the dataset are not totally labelled, in,¹⁹ they manually re-annotated the GT. Annotating the abnormal areas in pathology images are time-consuming, so, we focus on taking full advantages of the already labelled areas provided in the dataset, which we use higher order potentials for obtaining abundant contextual information to build up our HCRF model and automatically transfer the pixel-level GT to patch-level GT for a patch-level training. In,²¹ they also use a partially labelled dataset and they do not manually re-draw the GT either. Instead, they choose a multi-around training strategy to train the CNN while fully using already existing information in their dataset.

5.2 Mis-segmentation Analysis

There is still a big gap of the mis-segmentation problems to overcome. To analyse the mis-segmentation reasons, we give an example in Fig. 17.

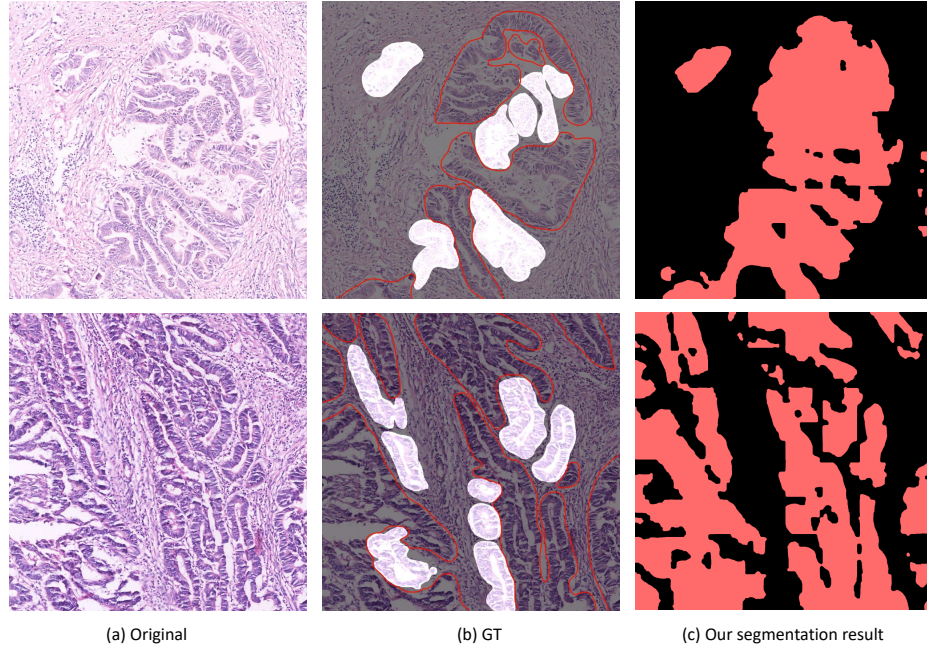


Fig 17 Typical examples of the mis-segmentation results. (a) presents the original images. (b) denotes the GT images. (c) shows the mis-segmentation results. The regions in the red curves in (b) are the positive regions in the redrawn GT images.

According to Fig. 17 and the medical knowledge from our cooperative histopathologists, the reasons for image segmentation errors are as follows:

(1) Fig. 17(a) reveals that the contents of the gastric histopathological images are complicated, in which the characteristics between normal and abnormal areas are always hard to distinguish, leading to a barrier in feature extraction or image content description.

(2) As shown in Fig. 17(b), when the abnormal regions in a gastric histopathological image are too many, the medical doctors drew the GT images roughly, where they did not figure out all of the abnormal regions. This low quality operation makes some positive regions to be labelled as negative, adding a training difficulty.

(3) From Fig. 17(b) and (c), we can find that, when we evaluate the segmentation results, our HCRF model may segment the positive regions correctly, but the original GT images may miss the corresponding regions. We consult our cooperative histopathologists and use red curves to roughly

redraw the regions that the original dataset did not label, where we can see that the original GT images in the applied dataset miss quite a lot of positive regions. It is obviously that the foreground of our segmentation result is more close to the redrawn GT images, but not the original GT images, and this case could lead to a low IoU and high SVD.

6 Conclusion and Future Work

In this research, we introduced a HCRF model to accomplish the gastric histopathology image segmentation task. This HCRF model not only uses traditional unary and binary potentials, but also applies higher order potentials to improve the segmentation quality. In pixel-level potentials, we retrain the U-Net; in patch-level potentials, we fine-tune the VGG-16, Inception-V3 and ResNet-50 networks. Furthermore, when jointing the pixel-level and patch-level potentials, we use different weights for different potentials to optimize the model. In the experiment, our HCRF model is finally evaluated on a gastric H&E histopathological test set and obtains a 78.91% segmentation accuracy, which is nearly close to the 79.83% segmentation accuracy on the validation set, showing the robustness and potential of our method.

In the future work, we plan to add more higher potentials, such as object detection potentials⁴⁶ to improve the segmentation quality. Meanwhile, we will add other state-of-the-art CNNs with different structures for more accurate segmentation results to our HCRF model.

Disclosures

The authors declare that there are no conflicts of interest related to the research presented in this article.

Acknowledgments

This work is supported by the “National Natural Science Foundation of China” (No. 61806047) and the “Fundamental Research Funds for the Central Universities” (No. N2019003).

References

- 1 B. Stewart and C. Wild, *World Cancer Report 2014*, World Health Organization, (UN) (2014).
- 2 E. Garcia, R. Hermoza, C. Castanon, *et al.*, “Automatic Lymphocyte Detection on Gastric Cancer IHC Images Using Deep Learning,” in *Proc. of CBMS 2017*, 200–204 (2017).
- 3 L. Srinidhi, O. Ciga, and L. Martel, “Deep neural network models for computational histopathology: A survey,” *arXiv preprint arXiv:1912.12378*, 1–45 (2019).
- 4 K. Simonyan and A. Zisserman, “Very deep convolutional networks for large-scale image recognition,” in *Proc. of ICLR 2015*, 1–14 (2015).
- 5 J. Long, E. Shelhamer, and T. Darrell, “Fully Convolutional Networks for Semantic Segmentation,” in *Proc. of ICPR 2015*, 3431–3440 (2015).
- 6 L. Chen, G. Papandreou, I. Kokkinos, *et al.*, “DeepLab: Semantic Image Segmentation with Deep Convolutional Nets, Atrous Convolution, and Fully Connected CRFs,” *IEEE Transactions on Pattern Analysis and Machine Intelligence* **40**(4), 834–848 (2018).
- 7 L. Hou, D. Samaras, T. Kurc, *et al.*, “Patch-based Convolutional Neural Network for Whole Slide Tissue Image Classification,” in *Proc. of CVPR 2016*, 2424–2433 (2016).
- 8 S. Li, “Markov Random Field Models in Computer Vision,” in *Proc. of ECCV 1994*, 361–370 (1994).
- 9 R. Gonzalez, R. Woods, and S. Eddins, *Digital Image Processing Using MATLAB*, Pearson Education, India (2004).

- 10 H. Sharma, N. Zerbe, D. Heim, *et al.*, “A Multi-resolution Approach for Combining Visual Information Using Nuclei Segmentation and Classification in Histopathological Images,” in *Proc. of VISAPP 2015*, 37–46 (2015).
- 11 T. Elsheikh, R. Austin, D. Chhieng, *et al.*, “American Society of Cytopathology Workload Recommendations for Automated Pap Test Screening: Developed by the Productivity and Quality Assurance in the Era of Automated Screening Task Force,” *Diagnostic Cytopathology* **41**(2), 174–178 (2013).
- 12 Y. LeCun, Y. Bengio, and G. Hinton, “Deep learning,” *Nature* **521**(7553), 436 (2015).
- 13 R. Lozano, “Comparison of Computer-assisted and Manual Screening of Cervical Cytology,” *Gynecologic Oncology* **104**(1), 134–138 (2007).
- 14 J. Qu, N. Hiruta, K. Terai, *et al.*, “Gastric pathology image classification using stepwise fine-tuning for deep neural networks,” *Journal of Healthcare Engineering* **2018**, 8961781 (2018).
- 15 S. Wienert, D. Heim, K. Saeger, *et al.*, “Detection and segmentation of cell nuclei in virtual microscopy images: a minimum-model approach,” *Scientific Reports* **2**, 503 (2012).
- 16 N. Kumar, R. Verma, S. Sharma, *et al.*, “A Dataset and a Technique for Generalized Nuclear Segmentation for Computational Pathology,” *IEEE Transactions on Medical Imaging* **36**(7), 1550–1560 (2017).
- 17 Y. Cui, G. Zhang, Z. Liu, *et al.*, “A deep learning algorithm for one-step contour aware nuclei segmentation of histopathology images,” *Medical & Biological Engineering & Computing* **57**(9), 2027–2043 (2019).
- 18 B. Peng, L. Chen, and J. Shang, M. and Xu, “Fully convolutional neural networks for tissue

- histopathology image classification and segmentation,” in *Proc. of ICIP 2018*, 1403–1407 (2018).
- 19 Y. Li, X. Xie, S. Liu, *et al.*, “Gt-net: A deep learning network for gastric tumor diagnosis,” in *Proc. of ICTAI 2018*, 20–24 (2018).
- 20 S. Wang, Y. Zhu, L. Yu, *et al.*, “Rmdl: Recalibrated multi-instance deep learning for whole slide gastric image classification,” *Medical Image Analysis* **58**, 101549 (2019).
- 21 Q. Liang, Y. Nan, G. Coppola, *et al.*, “Weakly supervised biomedical image segmentation by reiterative learning,” *IEEE Journal of Biomedical and Health Informatics* **23**(3), 1205–1214 (2019).
- 22 M. Sun, G. Zhang, H. Dang, *et al.*, “Accurate gastric cancer segmentation in digital pathology images using deformable convolution and multi-scale embedding networks,” *IEEE Access* **7**, 75530–75541 (2019).
- 23 X. He, R. Zemel, and M. Carreira-Perpiñán, “Multiscale Conditional Random Fields for Image Labeling,” in *Proc. of CVPR 2004*, **2**, 1–8 (2004).
- 24 J. Lafferty, A. McCallum, and F. Pereira, “Conditional Random Fields: Probabilistic Models for Segmenting and Labeling Sequence Data,” in *Proc. of ICML 2001*, 282–289 (2001).
- 25 F. Sha and F. Pereira, “Shallow Parsing with Conditional Random Fields,” in *Proc. of HLT-NAACL 2003*, 134–141 (2003).
- 26 B. Settles, “Biomedical Named Entity Recognition Using Conditional Random Fields and Rich Feature Sets,” in *Proc. of JNLPBA 2004*, 104–107 (2004).
- 27 K. Chang, T. Lin, L. Shih, *et al.*, “Analysis and Prediction of the Critical Regions of Antimicrobial Peptides Based on Conditional Random Fields,” *PloS One* **10**(3), e0119490 (2015).

- 28 S. Zheng, S. Jayasumana, B. Romera-Paredes, *et al.*, “Conditional Random Fields as Recurrent Neural Networks,” in *Proc. of ICCV 2015*, 1–17 (2015).
- 29 J. Ruiz-Sarmiento, C. Galindo, J. Gonzalez-Jimenez, *et al.*, “UPGMpp: A Software Library for Contextual Object Recognition,” in *Proc. of REACTS 2015*, 1–14 (2015).
- 30 Y. Wang and J. Rajapakse, “Contextual Modeling of Functional MR Images with Conditional Random Fields,” *IEEE Transactions on Medical Imaging* **25**(6), 804–812 (2006).
- 31 Y. Artan, M. Haider, D. Langer, *et al.*, “Prostate Cancer Localization with Multispectral MRI Using Cost-Sensitive Support Vector Machines and Conditional Random Fields,” *IEEE Transactions on Image Processing* **19**(9), 2444–2455 (2010).
- 32 S. Park, D. Sargent, R. Lieberman, *et al.*, “Domain-Specific Image Analysis for Cervical Neoplasia Detection Based on Conditional Random Fields,” *IEEE Transactions on Medical Imaging* **30**(3), 867–878 (2011).
- 33 D. Mary, V. Anandan, and K. Srinivasagan, “An Effective Diagnosis of Cervical Cancer Neoplasia by Extracting the Diagnostic Features Using CRF,” in *Proc. of ICCEET 2012*, 563–570 (2012).
- 34 S. Kosov, K. Shirahama, C. Li, *et al.*, “Environmental Microorganism Classification Using Conditional Random Fields and Deep Convolutional Neural Networks,” *Pattern Recognition* **77**, 248–261 (2018).
- 35 C. Li, H. Chen, D. Xue, *et al.*, “Weakly supervised cervical histopathological image classification using multilayer hidden conditional random fields,” in *Proc. of ITIB 2019*, 209–221 (2019).

- 36 O. Ronneberger, P. Fischer, and T. Brox, “U-net: Convolutional Networks for Biomedical Image Segmentation,” in *Proc. of MICCAI 2015*, 234–241 (2015).
- 37 C. Szegedy, W. Liu, Y. Jia, *et al.*, “Going Deeper with Convolutions,” in *Proc. of ICPR 2015*, 1–9 (2015).
- 38 S. Ioffe and C. Szegedy, “Batch normalization: Accelerating deep network training by reducing internal covariate shift,” in *Proc. of ICML 2015*, 448–456 (2015).
- 39 C. Szegedy, V. Vanhoucke, S. Ioffe, *et al.*, “Rethinking the Inception Architecture for Computer Vision,” in *Proc. of ICPR 2016*, 2818–2826 (2016).
- 40 K. He, X. Zhang, S. Ren, *et al.*, “Deep Residual Learning for Image Recognition,” in *Proc. of ICPR 2016*, 770–778 (2016).
- 41 T. Falk, D. Mai, R. Bensch, *et al.*, “U-net: Deep learning for cell counting, detection, and morphometry,” *Nature Methods* **16**(1), 67–70 (2019).
- 42 Ö. Çiçek, A. Abdulkadir, S. Lienkamp, *et al.*, “3D U-Net: Learning Dense Volumetric Segmentation from Sparse Annotation,” in *Proc. of MICCAI 2016*, 424–432 (2016).
- 43 P. Clifford, “Markov random fields in statistics; disorder in physical systems: A volume in honour of john m. hammersley,” *Oxford University Press* **19**, 32 (1990).
- 44 R. Gupta, “Conditional Random Fields.” Unpublished Report, IIT Bombay (2006).
- 45 V. Vineet, J. Warrell, and P. Torr, “Filter-based Mean-field Inference for Random Fields with Higher-Order Terms and Product Label-spaces,” in *Proc. of ECCV 2002*, 1–14 (2012).
- 46 A. Arnab, S. Jayasumana, S. Zheng, *et al.*, “Higher Order Conditional Random Fields in Deep Neural Networks,” in *Proc. of ECCV 2016*, 524–540 (2016).

- 47 O. Russakovsky, J. Deng, H. Su, *et al.*, “Imagenet Large Scale Visual Recognition Challenge,” *International Journal of Computer Vision* **115**(3), 211–252 (2015).
- 48 Y. Matsumoto, T. Shinozaki, K. Shirahama, *et al.*, “Kobe University, NICT and University of Siegen on the TRECVID 2016 AVS Task,” in *Proc. of TRECVID 2016*, 1–8 (2016).
- 49 S. Kumar and M. Hebert, “Discriminative Random Fields,” *International Journal of Computer Vision* **68**(2), 179–201 (2006).
- 50 D. Kermany, M. Goldbaum, W. Cai, *et al.*, “Identifying Medical Diagnoses and Treatable Diseases by Image-based Deep Learning,” *Cell* **172**(5), 1122–1131 (2018).
- 51 Y. Li, X. Li, X. Xie, *et al.*, “Deep learning based gastric cancer identification,” in *Proc. of ISBI 2018*, 182–185 (2018).
- 52 A. Garcia-Garcia, S. Orts-Escolano, S. Oprea, *et al.*, “A survey on deep learning techniques for image and video semantic segmentation,” *Applied Soft Computing* **70**, 41–65 (2018).
- 53 H. Chang, A. Zhuang, D. Valentino, *et al.*, “Performance Measure Characterization for Evaluating Neuroimage Segmentation Algorithms,” *Neuroimage* **47**(1), 122–135 (2009).
- 54 A. Taha and A. Hanbury, “Metrics for Evaluating 3D Medical Image Segmentation: Analysis, Selection, and Tool,” *BMC Medical Imaging* **15**(1), 29 (2015).
- 55 T. Heimann, B. Van Ginneken, A. Styner, *et al.*, “Comparison and evaluation of methods for liver segmentation from ct datasets,” *IEEE Transactions on Medical Imaging* **28**(8), 1251–1265 (2009).
- 56 D. Powers, “Evaluation: from Precision, Recall and F-measure to ROC, Informedness, Markedness and Correlation.” Technical Report in School of Informatics and Engineering, Flinders University, Adelaide, Australia, No. SIE-07-001 (2011).

- 57 C. Snoek, M. Worring, and A. Smeulders, “Early versus Late Fusion in Semantic Video Analysis,” in *Proc. of MM 2005*, 1–4 (2005).
- 58 M. Ingber and A. Mitra, “Grid Optimization for the Boundary Element Method,” *International Journal for Numerical Methods in Engineering* **23**(11), 2121–2136 (1986).
- 59 V. Badrinarayanan, A. Kendall, and R. Cipolla, “Segnet: A Deep Convolutional Encoder-decoder Architecture for Image Segmentation,” *IEEE Transactions on Pattern Analysis and Machine Intelligence* **39**(12), 2481–2495 (2017).
- 60 N. Otsu, “A Threshold Selection Method from Gray-level Histograms,” *IEEE Transactions on Systems, Man, and Cybernetics* **9**(1), 62–66 (1979).
- 61 L. Vincent and P. Soille, “Watersheds in Digital Spaces: An Efficient Algorithm based on Immersion Simulations,” *IEEE Transactions on Pattern Analysis and Machine Intelligence* **13**(6), 583–598 (1991).
- 62 J. Hartigan and M. Wong, “Algorithm AS 136: A k -means Clustering Algorithm,” *Journal of the Royal Statistical Society. Series C (Applied Statistics)* **28**(1), 100–108 (1979).

Changhao Sun received his B.E. degree in communication engineering from the Northeastern University, China, in 2018. Currently, he is a Master Student in the Research Group for Microscopic Image and Medical Image Analysis in the Northeastern University, China. His research interests are gastric histopathology image segmentation, conditional random fields and deep learning.

Chen Li received his Dr.- Ing. degree from the University of Siegen (1.0 score, MAGNA CUM LAUDE), Germany in 2016. From 2016 to 2017, he worked as a Postdoctoral Researcher in the

Johannes Gutenberg University Mainz, Germany. Currently, he is working as an Associate Professor in the Northeastern University, China. His research interests are microscopic image analysis, machine learning, pattern recognition, machine vision, multimedia retrieval and membrane computing.

Jinghua Zhang received his B.E. degree from Hefei University, PR China, in 2018. Currently, he is a Master Student in the Research Group for Microscopic Image and Medical Image Analysis in the Northeastern University, China. His research interests are microscopic image segmentation and deep learning.

Shiliang Ai received his B.Sc. degree from the Northeastern University, PR China, in 2016. From 2018 till now, he is a Master Student in the Research Group for Microscopic Image and Medical Image Analysis in the Northeastern University, China. His research interests are gastric histopathology image analysis and graph theory.

Hao Chen received his B.E. and M.E. degrees from the Northeastern University, China, in 2017 and 2019, respectively. He is a member of the Research Group for Microscopic Image and Medical. Currently, he is pursuing for his Doctor degree. His research interests include gastric histopathology image analysis, conditional random fields, feature extraction and image classification.

Frank Kulwa received his B.E. degree from the Dar es Salaam Institute of Technology, Tanzania, in 2013, where he has been a Tutorial Assistant, since 2017. Since 2018, he has been a Master Student with the Research Group for Microscopic Image and Medical Image Analysis, Northeastern University, China. His research interests include microscopic image segmentation and deep learning.

Xiaoyan Li received her Ph.D. degree in Pathology from China Medical University, China, in

2014. From 2014 till now, she works in the Department of Pathology, Cancer Hospital of China Medical University, Liaoning Cancer Hospital and Institute, engaged in the diagnosis of surgical tumor pathology and molecular pathology, and her main research direction is the occurrence and development mechanism of breast cancer and cervical cancer.

Tao Jiang received his Ph.D. degree from the University of Siegen, Germany, in 2013. He is currently a Full Professor with the Chengdu University of Information Technology (CUIT), China. He is also the Dean with the Control Engineering College of CUIT. His research interests include machine vision, artificial intelligence, robot control, self-driving auto, and membrane computing.